

Optimal Experiment Design for Magnetic Resonance Fingerprinting: Cramér-Rao Bound Meets Spin Dynamics

Bo Zhao, *Member, IEEE*, Justin P. Haldar, *Senior Member, IEEE*, Congyu Liao, Dan Ma, Mark A. Griswold, Kawin Setsompop, and Lawrence L. Wald, *Member, IEEE*

Abstract—Magnetic resonance (MR) fingerprinting is a new quantitative imaging paradigm, which simultaneously acquires multiple MR tissue parameter maps in a single experiment. In this work, we present a novel estimation-theoretic framework to perform optimal experiment design for MR fingerprinting. Specifically, we describe a discrete-time dynamic system to model spin dynamics, and derive the estimation-theoretic bound, i.e., Cramér-Rao bound (CRB), to characterize the signal-to-noise ratio (SNR) efficiency of an MR fingerprinting experiment. We further formulate an optimal experiment design problem, which selects a sequence of acquisition parameters to encode MR tissue parameters with the maximal SNR efficiency, while respecting the physical constraints and other constraints from the image decoding/reconstruction process. We evaluate the performance of the proposed approach with numerical simulations and phantom experiments, and demonstrate that the optimized experiments substantially reduce data acquisition time and/or improve parameter estimation accuracy. For example, the optimized experiments achieve about a factor of two improvement in the accuracy of T_2 maps, while keeping similar or slightly better accuracy of T_1 maps. Finally, as a remarkable observation, we find that the optimized acquisition parameters appears to be highly structured rather than randomly/pseudo-randomly varying as is prescribed in the conventional MR fingerprinting experiments.

Index Terms—Optimal experiment design, Cramér-Rao bound, spin dynamics, dynamic system, statistical inference, quantitative magnetic resonance imaging.

This work was partially supported by the National Institute of Health under Grant No. NIH-R01-EB017219 and NIH-R01-EB017337, and the National Science Foundation under Grant No. NSF-CCF-135063. B. Zhao was also supported by a Ruth L. Kirschstein National Research Service Award Postdoctoral Fellowship from the National Institute of Health under Grant No. NIH-F32-EB024381.

B. Zhao is with the Athinoula A. Martinos Center for Biomedical Imaging, Massachusetts General Hospital, Charlestown, MA 02129 USA, and also with the Department of Radiology, Harvard Medical School, Boston, MA 02115 USA (email: bzhao4@mgh.harvard.edu).

J. P. Haldar is with the Signal and Image Processing Institute and Ming Hsieh Department of Electrical Engineering, University of Southern California, Los Angeles, CA 90089 USA (jhalidar@usc.edu).

C. Liao is with the Athinoula A. Martinos Center for Biomedical Imaging, Massachusetts General Hospital, Charlestown, MA 02129 USA, and also with the Department of Biomedical Engineering, Zhejiang University, Hangzhou, Zhejiang Province 310027 China (email: cliao2@mgh.harvard.edu).

D. Ma and M. A. Griswold are with the Department of Radiology, Case Western Reserve University, Cleveland, OH 44106 USA (email: dan.ma@case.edu, mark.griswold@case.edu).

K. Setsompop and L. L. Wald are with the Athinoula A. Martinos Center for Biomedical Imaging, Massachusetts General Hospital, Charlestown, MA 02129 USA, and also with the Department of Radiology, Harvard Medical School, Boston, MA, 02115 USA, and also with the Harvard-MIT Division of Health Sciences and Technology, Massachusetts Institute of Technology, Cambridge, MA 02139 USA (email: kawin@nmr.mgh.harvard.edu, wald@nmr.mgh.harvard.edu).

I. INTRODUCTION

MAGNETIC resonance (MR) fingerprinting is a novel quantitative magnetic resonance imaging (MRI) framework [1]. It enables rapid acquisition of multiple MR tissue parameters (e.g., T_1 , T_2 , and spin density) in a single imaging experiment. Comparing to conventional MR relaxometry techniques (e.g., [2]–[5]), the original proof-of-principle MR fingerprinting implementation featured several key innovations in its encoding and decoding processes [1]. Specifically, during encoding, it applies a series of time-varying, random or quasi-random data acquisition parameters (e.g., flip angles and repetition times) to probe the spin system. This generates unique transient-state signal evolutions, or fingerprints, for different MR tissue parameters. It further applies incoherent spatial encoding (e.g., variable density spiral acquisition) to collect k-space data. During decoding, it performs a simple gridding reconstruction to reconstruct contrast-weighted images, after which it applies a dictionary-based pattern matching to obtain MR tissue parameter maps of interest.

Given its many departures from conventional quantitative imaging, some fundamental questions still remain unclear about the mechanism of MR fingerprinting. For example, from a theoretical perspective, the optimality of the encoding and decoding processes for MR fingerprinting have not been examined in [1]. While a recent work has performed a theoretical analysis of the MR fingerprinting problem from a low-dimensional manifold recovery viewpoint [6], this analysis is asymptotic and probabilistic in nature, and does not provide results that could be used to ensure the quality or guide the design of finite-duration MR fingerprinting experiments.

From a practical perspective, while existing MR fingerprinting methods work well in some scenarios, there are other important cases where the performance of these methods can be much worse. For example, the accuracy of T_2 maps from MR fingerprinting often depends critically on the length of data acquisition, and is much worse than the accuracy of T_1 maps, especially with short acquisition lengths [7]–[11]. In these settings, it would be highly desirable to either improve parameter mapping quality without increasing experiment duration, or reduce experiment duration without sacrificing parameter map quality.

Recently, we introduced a novel statistical imaging framework for MR fingerprinting [7], [8]. On the decoding side, we proposed a maximum likelihood (ML) reconstruction ap-

proach, which directly reconstructs MR tissue parameter maps from highly-undersampled, noisy k-space data. Moreover, we showed analytically that the conventional reconstruction approach in [1] is sub-optimal from a statistical estimation perspective [7], [8]. The use of ML reconstruction has dramatically improved the estimation accuracy and/or reduced acquisition time. Apart from the quality of image decoding schemes, the performance of MR fingerprinting inherently depends on the quality of the available data. This motivates us to explore the optimization of MR fingerprinting on the encoding side, which naturally falls into the domain of experiment design [12] in the statistical imaging framework.

In this paper, we address the optimal experiment design problem for MR fingerprinting. Our goal is to encode MR tissue parameters into the most informative measurements in the presence of noise. Specifically, we first model spin dynamics with a discrete-time dynamic system. We then calculate the estimation-theoretic bound, i.e., the Cramér-Rao bound (CRB) [13], as a measure of the signal-to-noise (SNR) efficiency for MR fingerprinting experiments. We further utilize this bound to formulate an optimal experiment design problem to choose MR fingerprinting acquisition parameters for the maximum SNR efficiency, while respecting both physical constraints and other constraints from image decoding. We show representative results from numerical simulations and phantom experiments to illustrate the performance of the optimized experiments. As a remarkable observation, we find that the sequence of optimized acquisition parameters appears to be highly structured rather than randomly/pseudo-randomly varying as used in the existing MR fingerprinting experiments (e.g., [1], [14]–[17]).

A preliminary account of this work was presented in our early conference papers [18], [19], which, to the best of our knowledge, first introduced the estimation-theoretic bound for MR fingerprinting experiment design. Recently, similar problems have also been investigated by other researchers. For example, Assländer et al. applied our approach to a new MR fingerprinting imaging sequence [15] under the polar coordinates of the Bloch equation [20]. Maidens et al. provided an optimal control interpretation of the experiment design problem, for which they developed a dynamic programming based algorithm [21]. However, due to the curse of dimensionality for dynamic programming [22], the feasibility of their approach was only demonstrated in a highly simplified scenario. Besides the CRB-based approaches, the experiment design problem was also addressed from other perspectives. For example, Cohen et al. optimized MR fingerprinting acquisition parameters by maximizing the discrimination power between different tissue types [23].

Note that the CRB has been previously used in analyzing and designing imaging experiments for conventional MR relaxometry (e.g., [24]–[32]). Here we extend these techniques to MR fingerprinting, which is a unique transient-state imaging approach that encodes MR tissue parameters into spin dynamics. In this context, the CRB calculation can be more complex, which requires handling a dynamic system, rather than an analytical signal model as in conventional MR relaxometry [24]–[32]. In this paper, we introduce an efficient way of

calculating the CRB for the Bloch equation based dynamic system. In particular, we show that the CRB calculation can be done by iterating a set of finite-difference equations with some given initializations.

For easy reference, we summarize here the key notations and symbols used in the paper. We use \mathbb{R} to denote the field of real numbers, and use \mathbb{R}^n and $\mathbb{R}^{m \times n}$ to respectively denote the space of real vectors of length n and the space of real $m \times n$ matrices. We use bold letters (e.g., \mathbf{x} or \mathbf{X}) to denote vectors or matrices. We respectively use \mathbf{X}^T , \mathbf{X}^{-1} , and $\text{tr}(\mathbf{X})$ to denote the transpose, inverse, and trace of \mathbf{X} . For a scalar-valued function $f : \mathbb{R}^N \rightarrow \mathbb{R}$ with the argument $\mathbf{x} \in \mathbb{R}^N$, we define its gradient, i.e., $\partial f / \partial \mathbf{x}$, as an $N \times 1$ vector with $[\partial f / \partial \mathbf{x}]_n = \partial f / \partial x_n$; for a vector-valued function $F : \mathbb{R}^N \rightarrow \mathbb{R}^M$ with the argument $\mathbf{x} \in \mathbb{R}^N$, we define its Jacobian matrix, i.e., $\partial F / \partial \mathbf{x}$, as an $M \times N$ matrix with $[\partial F / \partial \mathbf{x}]_{m,n} = \partial F_m / \partial x_n$; and for a matrix-valued function $\mathbf{F} : \mathbb{R} \rightarrow \mathbb{R}^{M \times N}$ with the argument $x \in \mathbb{R}$, we define its derivative an $M \times N$ matrix with $[\partial \mathbf{F} / \partial x]_{m,n} = \partial \mathbf{F}_{m,n} / \partial x$. For a random vector $\mathbf{x} \in \mathbb{R}^N$, we denote the expectation as $\mathbb{E}[\mathbf{x}] \in \mathbb{R}^N$, and the covariance matrix as $\text{Cov}(\mathbf{x}) = \mathbb{E}[(\mathbf{x} - \mathbb{E}(\mathbf{x}))(\mathbf{x} - \mathbb{E}(\mathbf{x}))^T] \in \mathbb{R}^{N \times N}$.

The rest of the paper is organized as follows. Section II presents the proposed approach in detail, which starts with a state-space model for spin dynamics, followed by the Cramér-Rao bound calculation and optimal design of MR fingerprinting experiments. Section III demonstrates the performance of the optimized MR fingerprinting experiments with numerical simulations and phantom experiments. Section IV discusses related issues and future work, followed by the concluding remarks in Section V.

II. PROPOSED APPROACH

A. Signal Model

There are a variety of MR fingerprinting imaging sequences that have recently been developed (e.g., [1], [14]–[17]). In this subsection, we start by formalizing a generic state-space model [33] for spin dynamics that underlie all MR fingerprinting experiments. We then give an example by specializing this model to a representative MR fingerprinting imaging sequence.

1) *State-Space Model*: Spin dynamics are governed by the Bloch equation [34], which is a system of first-order ordinary differential equations. While the magnetization evolves in continuous time, we are mainly interested in its values at a finite set of time points in an MR fingerprinting experiment. For convenience, we consider a discrete-time signal model, which should completely capture the features of interest for spin dynamics in continuous time. Moreover, here we focus on the magnetization evolution with respect to a small sample of tissue (i.e., a voxel); other issues related to spatial encoding will be discussed later.

In the presence of magnetic field inhomogeneity (e.g., with the use of gradients), intravoxel spin dephasing occurs. To account for this effect, we model multiple isochromats in an imaging voxel, each of which represents an ensemble of spins that have the same phase dispersions. Then we can use the isochromat-summation approach [35], [36] to approximate the magnetization evolution for the imaging voxel of interest.

Specifically, we first divide the voxel of interest, i.e., Δ , into a set of sufficiently small, equal-sized subvoxels $\{\Delta_{\mathbf{r}}\}$, where $\Delta_{\mathbf{r}}$ is centered at \mathbf{r} and $\Delta_{\mathbf{r}} \subset \Delta$. Here we assume that there exists a single isochromat for each $\Delta_{\mathbf{r}}$. We then analyze the magnetization evolution for each $\Delta_{\mathbf{r}}$. Finally, we obtain the overall magnetization for Δ by summing up all the magnetizations associated with the constituent subvoxels. Note that the above approach is general enough, in that it encompasses the special case that there exists only a single isochromat for the entire imaging voxel, i.e., all the subvoxels have the same phase dispersions.

We start by describing the magnetization evolution for each isochromat. Let $\mathbf{M}_{\mathbf{r}}[n] \in \mathbb{R}^3$ denote the magnetization associated with the isochromat for $\Delta_{\mathbf{r}}$ at the end of the n th repetition time (immediately before the next signal excitation). Here we can describe the magnetization evolution by the following state equation:

$$\mathbf{M}_{\mathbf{r}}[n] = \mathbf{A}_{\mathbf{r}}(\mathbf{u}[n], \boldsymbol{\theta})\mathbf{M}_{\mathbf{r}}[n-1] + \mathbf{B}_{\mathbf{r}}(\mathbf{u}[n], \boldsymbol{\theta}), \quad (1)$$

for $n = 1, \dots, N$, where $\boldsymbol{\theta} \in \mathbb{R}^p$ contains the unknown parameters in an MR fingerprinting experiment, including the tissue-specific parameters (e.g., T_1 , T_2 , and spin density) and experiment-specific parameters (e.g., off-resonance frequency); $\mathbf{u}[n] \in \mathbb{R}^q$ contains the data acquisition parameters applied during the n th repetition time, including the flip angle α_n , the phase of the radio frequency (RF) pulse ϕ_n , the echo time TE_n , and the repetition time TR_n ; $\mathbf{A}_{\mathbf{r}}(\mathbf{u}[n], \boldsymbol{\theta}) \in \mathbb{R}^{3 \times 3}$ and $\mathbf{B}_{\mathbf{r}}(\mathbf{u}[n], \boldsymbol{\theta}) \in \mathbb{R}^{3 \times 1}$ respectively denote the system matrix and input matrix for the n th repetition time. Note that in (1), we implicitly assume that all the subvoxels share the same set of parameters $\boldsymbol{\theta}$. Assuming that the imaging experiment starts from thermal equilibrium, the initial condition for (1) is given by $\mathbf{M}_{\mathbf{r}}[0] = [0, 0, M_0(\mathbf{r})]^T$, where $M_0(\mathbf{r}) = M_0/N_v$ denotes the magnitude of the magnetization for the subvoxel $\Delta_{\mathbf{r}}$ at thermal equilibrium, M_0 denotes the magnitude of magnetization for the entire imaging voxel Δ at thermal equilibrium, and N_v denotes the number of the sub-voxels in Δ .

The magnetization is measured at the corresponding echo time (i.e., TE_n) after each RF pulse excitation. The signal detected by the receiver coil is proportional to the transverse component of the magnetization. Denoting $\mathbf{m}_{\mathbf{r}}[n] \in \mathbb{R}^2$ as the transverse magnetization associated with $\Delta_{\mathbf{r}}$ at the n th echo time, we have

$$\mathbf{m}_{\mathbf{r}}[n] = \mathbf{C}_{\mathbf{r}}(\mathbf{u}[n], \boldsymbol{\theta})\mathbf{M}_{\mathbf{r}}[n-1], \quad (2)$$

for $n = 1, \dots, N$, where $\mathbf{C}_{\mathbf{r}}(\mathbf{u}[n], \boldsymbol{\theta}) \in \mathbb{R}^{2 \times 3}$ denotes the output matrix. Summing up all the magnetizations for each $\Delta_{\mathbf{r}}$, we can obtain the overall transverse magnetization for Δ as follows:

$$\mathbf{m}[n] = \sum_{\mathbf{r}: \Delta_{\mathbf{r}} \subset \Delta} \mathbf{m}_{\mathbf{r}}[n]. \quad (3)$$

Putting together (2) and (3), we have

$$\mathbf{m}[n] = \sum_{\mathbf{r}: \Delta_{\mathbf{r}} \subset \Delta} \mathbf{C}_{\mathbf{r}}(\mathbf{u}[n], \boldsymbol{\theta})\mathbf{M}_{\mathbf{r}}[n-1]. \quad (4)$$

The equations (1) and (4) together form a state-space model, which can describe spin dynamics for various MR

fingerprinting imaging sequences (e.g., [1], [14], [15], [17]). Note that this model is nonlinear and time-varying in nature.

2) *Example Sequence:* As an example, we illustrate the above state-space model using a widely-used MR fingerprinting pulse sequence, i.e., inversion recovery fast imaging with steady-state precession (IR-FISP) sequence [16]. Note that this sequence is robust to off-resonance effects with the use of dephasing gradients. Here the unknown parameters $\boldsymbol{\theta} = [T_1, T_2, M_0]^T$,¹ and the acquisition parameters $\mathbf{u}[n] = [\alpha_n, \phi_n, TE_n, TR_n]^T$.

In the IR-FISP sequence, three physical processes drive the magnetization evolutions: (1) RF excitation; (2) spin relaxation; and (3) spin dephasing. Here we use the isochromat-summation approach described above to model the intravoxel spin dephasing induced by the dephasing gradients. Specifically, under the Cartesian coordinates in the rotating frame [37],² we can form the system matrix $\mathbf{A}_{\mathbf{r}}$ as

$$\mathbf{A}_{\mathbf{r}}(\mathbf{u}[n], \boldsymbol{\theta}) = \mathbf{G}(\beta_{\mathbf{r}})\mathbf{R}(T_1, T_2, TR_n)\mathbf{Q}(\alpha_n, \phi_n), \quad (5)$$

where $\mathbf{Q}(\alpha_n, \phi_n) \in \mathbb{R}^{3 \times 3}$ models the RF excitation, i.e.,

$$\mathbf{Q}(\alpha_n, \phi_n) = \begin{bmatrix} \cos(\phi_n) & \sin(\phi_n) & 0 \\ -\sin(\phi_n) & \cos(\phi_n) & 0 \\ 0 & 0 & 1 \end{bmatrix} \begin{bmatrix} 1 & 0 & 0 \\ 0 & \cos(\alpha_n) & \sin(\alpha_n) \\ 0 & -\sin(\alpha_n) & \cos(\alpha_n) \end{bmatrix} \begin{bmatrix} \cos(\phi_n) & -\sin(\phi_n) & 0 \\ \sin(\phi_n) & \cos(\phi_n) & 0 \\ 0 & 0 & 1 \end{bmatrix};$$

$\mathbf{R}(T_1, T_2, t) \in \mathbb{R}^{3 \times 3}$ models the spin relaxation, i.e.,

$$\mathbf{R}(T_1, T_2, t) = \begin{bmatrix} e^{-t/T_2} & 0 & 0 \\ 0 & e^{-t/T_2} & 0 \\ 0 & 0 & e^{-t/T_1} \end{bmatrix};$$

and $\mathbf{G}(\beta_{\mathbf{r}}) \in \mathbb{R}^{3 \times 3}$ models the spin dephasing, i.e.,

$$\mathbf{G}(\beta_{\mathbf{r}}) = \begin{bmatrix} \cos(\beta_{\mathbf{r}}) & \sin(\beta_{\mathbf{r}}) & 0 \\ -\sin(\beta_{\mathbf{r}}) & \cos(\beta_{\mathbf{r}}) & 0 \\ 0 & 0 & 1 \end{bmatrix},$$

where $\beta_{\mathbf{r}}$ denotes the phase dispersion associated with the isochromat at $\Delta_{\mathbf{r}}$. Note that in the IR-FISP sequence, $\beta_{\mathbf{r}}$ is dominated by the impact of dephasing gradients, although there are various other factors (e.g., diffusion effect) that can also contribute to spin dephasing.

Moreover, we can form the input matrix $\mathbf{B}_{\mathbf{r}}$ as

$$\mathbf{B}_{\mathbf{r}}(\mathbf{u}[n], \boldsymbol{\theta}) = M_0(\mathbf{r})\mathbf{b}(T_1, TR_n), \quad (6)$$

where $\mathbf{b}(T_1, t) = [0, 0, 1 - e^{-t/T_1}]^T$. Note that $\mathbf{B}_{\mathbf{r}}(\mathbf{u}[n], \boldsymbol{\theta})$ models the recovery of the longitudinal magnetization.

Finally, we can form the output matrix $\mathbf{C}_{\mathbf{r}}$ as

$$\mathbf{C}_{\mathbf{r}}(\mathbf{u}[n], \boldsymbol{\theta}) = \mathbf{P}\mathbf{R}(T_1, T_2, TE_n)\mathbf{Q}(\alpha_n, \phi_n), \quad (7)$$

¹Note that M_0 is proportional to the spin density at Δ [37]. Here the scaling constant depends on the field strength, the temperature of the spin system, the gyromagnetic ratio, etc.

²Alternatively, the model can be described in other coordinate systems (e.g., the polar coordinates [20]); however, note that the Cramér-Rao bound does not change under any transform of the coordinate system for the Bloch equations.

where $\mathbf{P} \in \mathbb{R}^{2 \times 3}$ is the projection matrix that extracts the transverse magnetization, i.e.,

$$\mathbf{P} = \begin{bmatrix} 1 & 0 & 0 \\ 0 & 1 & 0 \end{bmatrix},$$

and $\mathbf{R}(T_1, T_2, TE_n)$ and $\mathbf{Q}(\alpha_n, \phi_n)$ are defined in the same way as before. Note that $\mathbf{C}_r(\mathbf{u}[n], \boldsymbol{\theta})$ models the RF excitation as well as the spin relaxation. Note that this matrix does not account for spin dephasing, since the dephasing gradient is placed after the echo time for each repetition time.

B. Cramér-Rao Bound

We proceed to describe the data model, with which we calculate the CRB and perform experiment design. Note that the spin dynamics described above are utilized to perform contrast encoding in MR fingerprinting experiments. Besides the contrast encoding, the data generating process also encompasses spatial encoding and noise contamination. In [7], [8], we described a data model for this data generating process. In principle, we can use it to calculate the CRB and perform experiment design. In practice, however, this can be computationally very expensive with the use of the nonCartesian Fourier transform for spatial encoding. Here we describe a practical approach, in which we ignore the spatial encoding, and use the following simplified data model:

$$\mathbf{s}[n] = \mathbf{m}[n] + \mathbf{z}[n], \quad (8)$$

for $n = 1, \dots, N$. Here $\mathbf{s}[n] \in \mathbb{R}^2$ is a vector that contains the magnetizations collected at the n th echo time, and $\{\mathbf{z}[n]\}_{n=1}^N$ denotes independent, identically distributed Gaussian noise with $\mathbf{z}[n] \sim N(\mathbf{0}, \sigma^2 \mathbf{I})$. Note that (8) corresponds to the data model for a single voxel nuclear magnetic resonance (NMR) experiment. Alternatively, it can also be viewed as the data model for a fully-sampled imaging experiment,³ in which there is no ‘‘crosstalk’’ between magnetization evolutions at different voxels. Despite such simplification, we will demonstrate later that the experiment design with (8) can be very effective for highly-undersampled MR fingerprinting experiments.

Next, we derive the CRB with (8). From estimation theory, the CRB provides a lower bound on the covariance of any unbiased estimator under mild regularity conditions, and it can be asymptotically achieved by the ML estimator [13]. Mathematically, we can express the CRB in the following information inequality [13]:

$$\mathbb{E} \left\{ \left(\boldsymbol{\theta} - \hat{\boldsymbol{\theta}} \right) \left(\boldsymbol{\theta} - \hat{\boldsymbol{\theta}} \right)^T \right\} \geq \mathbf{V}(\boldsymbol{\theta}) = \mathbf{I}^{-1}(\boldsymbol{\theta}), \quad (9)$$

for any unbiased estimator $\hat{\boldsymbol{\theta}}$, where $\mathbf{I}(\boldsymbol{\theta}) \in \mathbb{C}^{p \times p}$ denotes the Fisher information matrix (FIM) defined as [13]:

$$\mathbf{I}(\boldsymbol{\theta}) = \mathbb{E} \left[\left(\frac{\partial \ln p(\{\mathbf{s}[n]\}; \boldsymbol{\theta})}{\partial \boldsymbol{\theta}} \right) \left(\frac{\partial \ln p(\{\mathbf{s}[n]\}; \boldsymbol{\theta})}{\partial \boldsymbol{\theta}} \right)^T \right],$$

$\mathbf{V}(\boldsymbol{\theta}) \in \mathbb{C}^{p \times p}$ denotes the CRB matrix, and $\ln p(\mathbf{x}; \boldsymbol{\theta})$ denotes the log-likelihood function of the observation \mathbf{x} parameterized

³More precisely, this is equivalent to a single-channel Nyquist-sampled Cartesian Fourier acquisition with a discrete Fourier transform based image reconstruction.

by $\boldsymbol{\theta}$. In (9), the matrix inequality $\mathbf{A} \geq \mathbf{B}$ means that $\mathbf{A} - \mathbf{B}$ is a positive semidefinite matrix. Note that both the CRB and FIM depend on the underlying tissue parameter $\boldsymbol{\theta}$, given that the data model (8) is a nonlinear with respect to $\boldsymbol{\theta}$. Moreover, we can obtain the bound on the variance of individual tissue parameter estimate by extracting the corresponding diagonal entry of the CRB matrix, i.e.,

$$\text{Var}(\hat{\boldsymbol{\theta}}_i) \geq [\mathbf{V}(\boldsymbol{\theta})]_{i,i}. \quad (10)$$

To calculate the CRB in (9), we need to compute the FIM $\mathbf{I}(\boldsymbol{\theta})$. First, noting that $\mathbf{I}(\boldsymbol{\theta})$ is additive for the independent measurements $\{\mathbf{s}[n]\}_{n=1}^N$, we have

$$\mathbf{I}(\boldsymbol{\theta}) = \sum_{n=1}^N \mathbf{I}_n(\boldsymbol{\theta}), \quad (11)$$

where $\mathbf{I}_n(\boldsymbol{\theta})$ is the FIM associated with $\mathbf{s}[n]$, i.e.,

$$\mathbf{I}_n(\boldsymbol{\theta}) = \mathbb{E} \left[\left(\frac{\partial \ln p(\mathbf{s}[n]; \boldsymbol{\theta})}{\partial \boldsymbol{\theta}} \right) \left(\frac{\partial \ln p(\mathbf{s}[n]; \boldsymbol{\theta})}{\partial \boldsymbol{\theta}} \right)^T \right].$$

Second, for the Gaussian data model in (8), the FIM has the particularly simple form, which can be written as follows [13]:

$$\mathbf{I}_n(\boldsymbol{\theta}) = \frac{1}{\sigma^2} \mathbf{J}_n^T(\boldsymbol{\theta}) \mathbf{J}_n(\boldsymbol{\theta}), \quad (12)$$

where $\mathbf{J}_n(\boldsymbol{\theta}) = \partial \mathbf{m}[n] / \partial \boldsymbol{\theta} \in \mathbb{C}^{2 \times p}$ is the Jacobian matrix. Putting together (11) and (12), we have

$$\mathbf{I}(\boldsymbol{\theta}) = \frac{1}{\sigma^2} \sum_{n=1}^N \mathbf{J}_n^T(\boldsymbol{\theta}) \mathbf{J}_n(\boldsymbol{\theta}). \quad (13)$$

Finally, we describe the calculation of $\mathbf{J}_n(\boldsymbol{\theta})$ for (13). Given the state-space model in (1) and (4), such calculation is equivalent to solving a set of finite difference equations via recursion. More specifically, noting that

$$\mathbf{J}_n(\boldsymbol{\theta}) = \frac{\partial \mathbf{m}[n]}{\partial \boldsymbol{\theta}} = \begin{bmatrix} \frac{\partial}{\partial \theta_1} \mathbf{m}[n] & \cdots & \frac{\partial}{\partial \theta_p} \mathbf{m}[n] \end{bmatrix}, \quad (14)$$

we can compute $\partial \mathbf{m}[n] / \partial \theta_i$ for each entry of $\boldsymbol{\theta}$. This can be done as follows. First, we invoke the derivative with respect to θ_i on both sides of (4), which yields

$$\frac{\partial \mathbf{m}[n]}{\partial \theta_i} = \sum_{\mathbf{r}: \Delta_r \subset \Delta} \left\{ \frac{\partial \mathbf{C}_r(\mathbf{u}[n], \boldsymbol{\theta})}{\partial \theta_i} \mathbf{M}_r[n-1] + \mathbf{C}_r(\mathbf{u}[n], \boldsymbol{\theta}) \frac{\partial \mathbf{M}_r[n-1]}{\partial \theta_i} \right\}, \quad (15)$$

for $n = 1, \dots, N$. Then we invoke the derivative with respect to θ_i on both sides of (1), which yields

$$\begin{aligned} \frac{\partial \mathbf{M}_r[n]}{\partial \theta_i} &= \frac{\partial \mathbf{A}_r(\mathbf{u}[n], \boldsymbol{\theta})}{\partial \theta_i} \mathbf{M}_r[n-1] \\ &+ \mathbf{A}_r(\mathbf{u}[n], \boldsymbol{\theta}) \frac{\partial \mathbf{M}_r[n-1]}{\partial \theta_i} + \frac{\partial \mathbf{B}_r(\mathbf{u}[n], \boldsymbol{\theta})}{\partial \theta_i}. \end{aligned} \quad (16)$$

Now we can iterate the two finite difference equations (15) and (16) to calculate $\frac{\partial}{\partial \theta_i} \mathbf{m}[n]$. Note that the initial conditions are given by $\mathbf{M}_r[0] = [0, 0, M_0(\mathbf{r})]^T$ and $\partial \mathbf{M}_r[0] / \partial \theta_i = [0, 0, \partial M_0(\mathbf{r}) / \partial \theta_i]^T$. For the sake of concreteness, in the Appendix, we illustrate the above procedure with the example IR-FISP sequence.

C. Optimal Experiment Design

Given that the CRB provides a lower bound on the smallest possible variance for any unbiased estimator, we can use it to characterize the SNR efficiency. This helps understand the potential reliability of an MR fingerprinting experiment, and figure out how much acquisition time is necessary to achieve a certain level of quantitative accuracy. More importantly, we can use the CRB as a principled tool to optimize the encoding process of an MR fingerprinting experiment. Specifically, given a set of representative MR tissue parameters $\{\boldsymbol{\theta}^{(l)}\}_{l=1}^L$, we can optimize data acquisition parameters of an MR fingerprinting experiment to maximize its SNR efficiency. Mathematically, we can formulate the following experiment design problem:

$$\begin{aligned} \min_{\mathbf{u}} \quad & \sum_{l=1}^L \Psi(\mathbf{V}(\boldsymbol{\theta}^{(l)})) \\ \text{s.t.} \quad & \mathbf{u} \in \mathcal{U}, \end{aligned} \quad (17)$$

where $\Psi(\cdot)$ denotes the design criterion, which is a scalar function of the CRB matrix; $\mathbf{u} = [\mathbf{u}[1], \dots, \mathbf{u}[N]] \in \mathbb{C}^{q \times N}$ denotes the acquisition parameters for an MR fingerprinting experiment with N time points; and $\mathcal{U} \subset \mathbb{C}^{q \times N}$ denotes the constraint set for feasible data acquisition parameters.

Note that in (17), we assume that the total number of time points, i.e., N , is given. In practice, N can be specified according to the desired experiment duration. Moreover, given that the CRB matrix depends on the underlying tissue parameter, we assume that, for a specific imaging application of interest (e.g., neuroimaging), we have the knowledge of the range of MR tissue parameter values prior to our experiment design. While it is desirable to design experiments that are universally optimal for all possible parameters within the range, this is often not feasible. As such, we select a few representative tissues as a practical compromise.

As an example, we specialize (17) to optimize MR fingerprinting experiments with the example IR-FISP sequence. First, we specify the design criterion for $\Psi(\cdot)$. Note that there are various information criteria that can be used, including the A-optimality, D-optimality, and E-optimality criteria (see [12] for a comprehensive survey). Here we choose the A-optimality criterion [12], which minimizes the trace of the CRB matrix (i.e., the total variance of tissue parameter estimates). Further, we incorporate weightings into the design criterion, which is motivated by: (1) the CRBs for different tissue parameters are often at very different scales; and (2) we may want to tailor a design to the parameters that are most relevant to specific applications of interest. Accordingly, we have $\Psi(\cdot) = \text{tr}(\mathbf{W}\mathbf{V}(\boldsymbol{\theta}))$, where \mathbf{W} is a diagonal matrix whose entries contain weightings for different tissue parameters.

Second, we specify the data acquisition parameters $\mathbf{u} = [\mathbf{u}[1], \dots, \mathbf{u}[N]]$. Note that the acquisition parameters for the IR-FISP sequence include the flip angles, RF pulse phases, echo times, and repetition times. Following the early work [14], we assume the flip angles and repetition times to be the design parameters, while fixing the RF pulse phases and echo times. Accordingly, we have $\mathbf{u}[n] = [\alpha_n, TR_n]^T$, for $n = 1, \dots, N$.

Lastly, we specify the constraint set \mathcal{U} for the acquisition parameters. Taking into account various physical considerations (e.g., specific absorption rate (SAR), and/or total acquisition time), we impose upper bounds and lower bounds for the acquisition parameters, i.e., $TR_n \in [TR_n^{\min}, TR_n^{\max}]$, and $\alpha_n \in [\alpha_n^{\min}, \alpha_n^{\max}]$, for $n = 1, \dots, N$. Accordingly, we can formulate the experiment design problem as follows:

$$\begin{aligned} \min_{\{\alpha_n, TR_n\}} \quad & \sum_{l=1}^L \text{tr}(\mathbf{W}\mathbf{V}(\boldsymbol{\theta}^{(l)})) \\ \text{s.t.} \quad & TR_n^{\min} \leq TR_n \leq TR_n^{\max}, \quad 1 \leq n \leq N, \\ & \alpha_n^{\min} \leq \alpha_n \leq \alpha_n^{\max}, \quad 1 \leq n \leq N. \end{aligned} \quad (18)$$

Besides the physical constraints, it is often useful to take into account other constraints from image decoding/reconstruction, especially when dealing with highly-undersampled MR fingerprinting experiments. While different reconstruction methods may use different strategies for image decoding (from highly-undersampled data), they often benefit from magnetization evolutions being smoothly varying.⁴ There are a number of ways to enforce this property. Here we incorporate an additional set of constraints into (18), which restricts the maximum flip angle variations between consecutive time points. As will be demonstrated later, such constraints are effective in promoting smooth magnetization evolutions, which yields better performance for image reconstruction with highly-undersampled data. Accordingly, we can formulate the experiment design problem as follows:

$$\begin{aligned} \min_{\{\alpha_n, TR_n\}_{n=1}^N} \quad & \sum_{l=1}^L \text{tr}(\mathbf{W}\mathbf{V}(\boldsymbol{\theta}^{(l)})) \\ \text{s.t.} \quad & TR_n^{\min} \leq TR_n \leq TR_n^{\max}, \quad 1 \leq n \leq N, \\ & \alpha_n^{\min} \leq \alpha_n \leq \alpha_n^{\max}, \quad 1 \leq n \leq N, \\ & |\alpha_{n+1} - \alpha_n| \leq \Delta\alpha_n^{\max}, \quad 1 \leq n \leq N-1. \end{aligned} \quad (19)$$

where $\Delta\alpha_n^{\max}$ specifies the maximum flip angle variations between α_n and α_{n+1} .

The proposed formulations in (18) and (19) result in nonlinear and nonconvex optimization problems. A number of algorithms can be employed to solve these optimization problems, including standard nonlinear optimization methods [39] and stochastic optimization methods [40]. As an example, we use a state-of-the-art nonlinear optimization method, i.e., sequential quadratic programming (SQP) [39], to seek local minima for (18) and (19). As with other nonlinear optimization methods, the performance of the SQP algorithm is generally dependent on initialization. Here we initialize the algorithm with the acquisition parameters from the conventional MR fingerprinting experiment [14], with which the algorithm consistently yields good performance, although other initialization schemes (e.g., a multi-start strategy) may lead to better performance.

⁴For example, for the conventional reconstruction method [1] that utilizes direct pattern matching, smooth magnetization evolutions can be better differentiated from aliasing artifacts, leading to improved accuracy in dictionary matching. As another example, for the low-rank/subspace reconstruction method [11], smooth magnetization evolutions often result in a smaller low-rank approximation error given the same rank value. This in turn enables better reconstruction accuracy. Finally, for the statistical reconstruction methods [8], [38], which involve solving nonconvex optimization problems, an initialization from the improved conventional reconstruction or low-rank reconstruction method often leads to better performance.

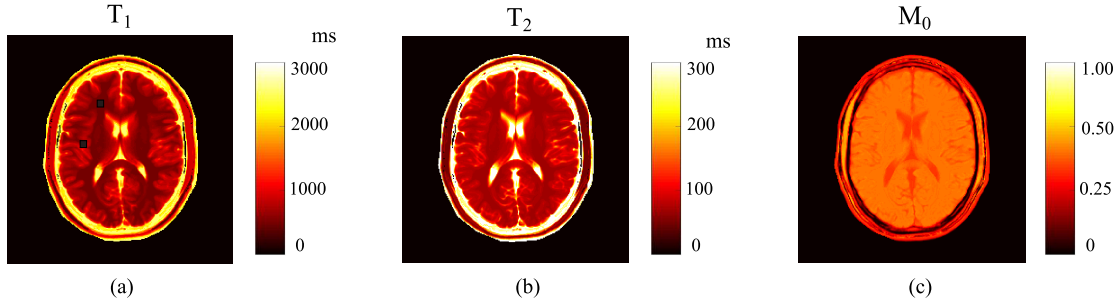


Fig. 1. Ground truth parameter maps for the brain phantom: (a) T_1 map, (b) T_2 map, and (c) M_0 map. Note that the two ROIs (respectively in the white matter and gray matter) are marked in (a).

III. RESULTS

In this section, we show representative results from numerical simulations and phantom experiments to illustrate the performance of the proposed method.

A. Simulations

1) *General Setup*: We created a numerical brain phantom to simulate single-channel MR fingerprinting experiments. We took the T_1 , T_2 , and M_0 maps from the Brainweb database [41] as the ground truth, as shown in Fig. 1. We set the experimental field-of-view (FOV) as $300 \times 300 \text{ mm}^2$, and the matrix size as 256×256 . We simulated MR fingerprinting experiments with the IR-FISP sequence [14], which is robust to main magnetic field inhomogeneity. Moreover, for simplicity, we assumed that the transmit RF field was homogeneous in the simulations.

We performed Bloch simulations to generate contrast-weighted images. Here we used the isochromat-summation approach [35], [36], in which we simulated magnetization evolutions with 400 isochromats for each voxel.⁵ In Bloch simulations, we considered three different sets of acquisition parameters: (1) the conventional scheme [14], (2) the optimized scheme with (18), and (3) the optimized scheme with (19). In Fig. 2, we show the acquisition parameters from the conventional scheme with $N = 1000$, as well as the resulting magnetization evolutions for the two ROIs, respectively, in the white matter tissue and a gray matter tissue (as marked in Fig. 1 (a)).

We generated k-space data from the contrast-weighted images using the non-uniform Fourier transform [43]. In the simulations, we considered two setups of MR fingerprinting experiments:

- Fully-sampled experiment: we acquired fully-sampled Cartesian k-space data for each time point (or TR index), as in [44].
- Highly-undersampled experiment: we acquired highly-undersampled spiral k-space data at each time point, as in [14]. For this, we used the same spiral trajectory as [14], and acquired only one spiral interleaf for each time

⁵Note that the accuracy of this approach depends on the number of isochromats used in Bloch simulations [35], [36]. Here with a total number of 400 isochromats, we can obtain very good accuracy, compared to the extended phase graph formalism [42].

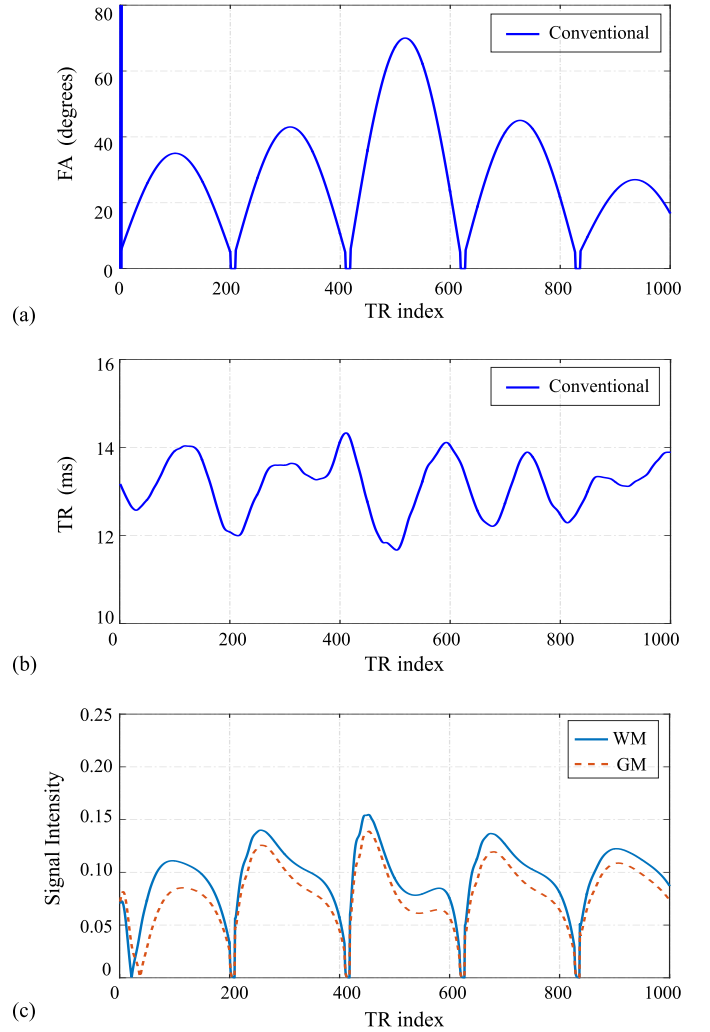


Fig. 2. Acquisition parameters of the conventional scheme with $N = 1000$ as well as the resulting magnetization evolutions. (a) Flip angle train. (b) Repetition time train. (c) Magnetization evolutions for the white matter and gray matter ROIs marked in Fig. 1 (a). Note that the first RF pulse is 180° , which exceeds the scale of the vertical axes in (a).

point, whereas a full set of spiral trajectory consists of 48 interleaves.

We added complex white Gaussian noise to the measured k-space data according to the pre-specified noise level σ^2 . Here

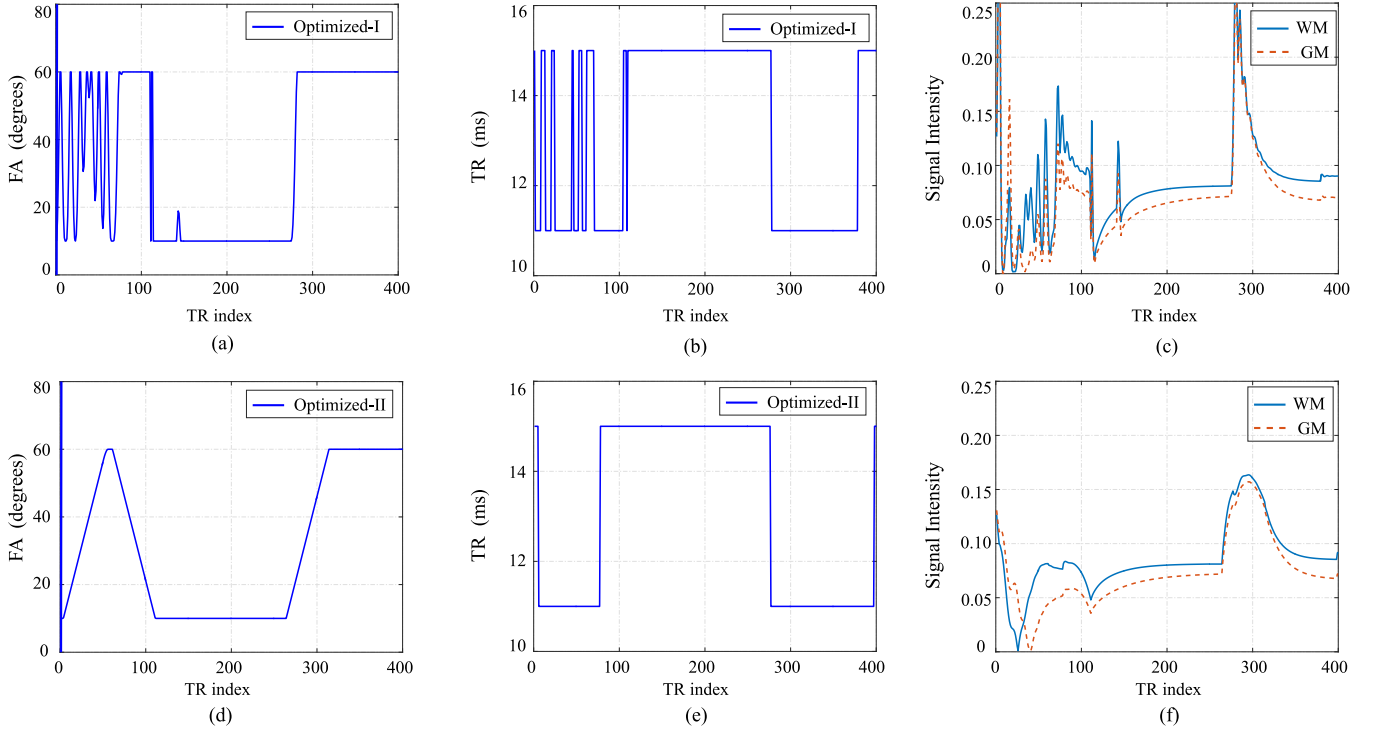


Fig. 3. Two optimized acquisition schemes with $N = 400$, and the resulting magnetization evolutions for the white matter and the gray matter ROIs marked in Fig. 1 (a). (a) Flip angle train in Optimized-I. (b) Repetition time train in Optimized-I. (c) Magnetization evolutions from Optimized-I. (d) Flip angle train in Optimized-II. (e) Repetition time train in Optimized-II. (f) Magnetization evolutions from Optimized-II. Note that the first RF pulses are 180° for both Optimized-I and Optimized-II, which exceed the scale of the vertical axes in (a) and (d).

we define the signal-to-noise ratio as $\text{SNR} = 20 \log_{10}(s/\sigma)$,⁶ where s denotes the average value of M_0 in a region of white matter. With this, we measure the SNR in decibels (dB).

We performed the ML reconstruction [7], [8] for the above experiments. Note that for the fully-sampled Cartesian experiments, the ML approach is equivalent to the direct Fourier reconstruction, followed by the dictionary-based pattern matching [45]. For the highly-undersampled experiments, we solved the reconstruction problem with the algorithm in [7], [8], which we initialized with the gridding reconstruction. Here the dictionary used in the ML reconstruction was constructed based on the following parameter discretization scheme: we set the T_1 value in the range $[20, 3000]$ ms, in which we used an increment of 10 ms for $[20, 1500]$ ms and an increment of 30 ms for $[1501, 3000]$ ms; we set the T_2 value in the range $[30, 500]$ ms, in which we used an increment of 1 ms for $[30, 200]$ ms and an increment of 5 ms for $[201, 500]$ ms.

To assess the reconstruction accuracy, we used the following two metrics: (a) overall error, i.e., $\|\mathbf{I} - \hat{\mathbf{I}}\|_2 / \|\mathbf{I}\|_2$, where \mathbf{I} and $\hat{\mathbf{I}}$ respectively denote the true parameter map and reconstructed parameter map, and (b) voxelwise relative error, i.e., $|\mathbf{I}_v - \hat{\mathbf{I}}_v| / |\mathbf{I}_v|$, where \mathbf{I}_v and $\hat{\mathbf{I}}_v$ respectively denote the values of \mathbf{I} and $\hat{\mathbf{I}}$ at the v th voxel.

2) *Implementation of (18) and (19)*: Here we describe the detailed implementation of the proposed approach for the above application example. For convenience, we refer to the optimized schemes with (18) and (19) as Optimized-I and

Optimized-II, respectively. In this work, we assumed that T_1 and T_2 were of primary interest, for which we manually chose the weighting matrix \mathbf{W} to ensure the good performance of the optimized experiments.⁷ Moreover, we chose three representative tissues, i.e., $\boldsymbol{\theta}^{(1)} = [700 \text{ ms}, 60 \text{ ms}, 0.6]$, $\boldsymbol{\theta}^{(2)} = [850 \text{ ms}, 50 \text{ ms}, 0.6]$, and $\boldsymbol{\theta}^{(3)} = [1100 \text{ ms}, 102 \text{ ms}, 0.6]$, for (18) and (19).⁸

We further specify the constraints for the acquisition parameters in (18) and (19). Here we set the maximum flip angle as

$$\alpha_n^{\max} = \begin{cases} 180^\circ, & \text{if } n = 1, \\ 60^\circ, & \text{if } 2 \leq n \leq N. \end{cases}$$

Note that this allows an 180° inversion pulse imposed at the beginning of imaging experiments, which is often advantageous for the T_1 estimation [19]. We set the minimum flip angle as $\alpha_n^{\min} = 10^\circ$ for $1 \leq n \leq N$. We respectively set the maximum and minimum repetition times as $TR_n^{\max} = 15 \text{ ms}$ and $TR_n^{\min} = 11 \text{ ms}$ for $1 \leq n \leq N$. Here, it is worth mentioning that the above constraints roughly match the range of the acquisition parameters in the conventional scheme. For (19), we have the additional constraints on the flip angle

⁷Note that the same weighting matrix \mathbf{W} was used for both (18) and (19), which facilitates the subsequent comparison.

⁸The T_1 and T_2 values of these tissues were arbitrarily chosen from the range of tissue parameter values that are relevant to neuroimaging. To avoid the inverse crime, we did not take tissue parameter values directly from the brain phantom.

⁶We use the above SNR definition throughout the paper, although there are various other ways of defining SNR in MRI.

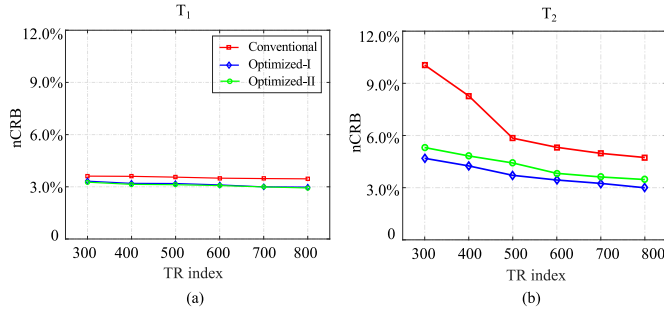


Fig. 4. Normalized CRB versus acquisition length for the ROI in the white matter tissue. (a) Normalized CRBs for T_1 . (b) Normalized CRBs for T_2 .

variations, which were set as

$$\Delta\alpha_n^{\max} = \begin{cases} +\infty, & \text{if } n = 1, \\ 1^\circ, & \text{if } 2 \leq n \leq N - 1. \end{cases}$$

Note that the above constraint does not restrict the flip angle variation between the inversion pulse and the second RF pulse.

We applied the SQP algorithm to solve the optimization problems associated with (18) and (19). As mentioned before, we initialized the algorithm with the acquisition parameters from the conventional scheme. We terminated the algorithm, when the change of the solution was less than the pre-specified tolerance (i.e., $\epsilon = 1e^{-4}$) or the maximum iteration (i.e., $J_{\max} = 5 \times 10^4$) was reached. The runtime of the algorithm depends on the length of acquisition. For example, with $N = 400$, solving (18) and (19) respectively took about 290 min and 140 min on a Linux workstation with 24 Intel Xeon E5-2643, 3.40 GHz processors and 128 GB RAM running Matlab R2015b.

We optimized the acquisition parameters independently for several choices of N (i.e., $N = 300, 400, 500, 600, 700$, and 800). As an example, Fig. 3 shows the optimized acquisition parameters with $N = 400$ from Optimized-I and Optimized-II. As can be seen, the optimized acquisition parameters appear to be highly structured, which are remarkably different from the acquisition parameters from the conventional scheme. In particular, the optimized repetition times turn out to be binary (i.e., switching between TR_n^{\max} and TR_n^{\min}). Besides $N = 400$, we also had similar observations for all other acquisition lengths. We show one more example, i.e., the optimized schemes with $N = 600$ in the supplementary material. In Section IV, we will have a detailed discussion on such an interesting observation.

Fig. 3 also shows the resulting magnetization evolutions from Optimized-I and Optimized-II. As can be seen, the magnetization evolutions from Optimized-I exhibit significant oscillation due to the dramatic change of acquisition parameters (within the first 100 time points). In contrast, by enforcing the additional constraints on the flip angle variations in Optimized-II, the oscillation behavior has been significantly suppressed, and the resulting magnetization evolutions appear to be much smoother. Later we will demonstrate that this is advantageous for image reconstruction from highly-undersampled data.

3) *Evaluation of CRB*: We evaluated the CRB for the conventional scheme, Optimized-I, and Optimized-II. Note that

the CRB is a lower bound on the variance (or equivalently, the mean-square error) of an unbiased estimator, which characterizes the SNR property of an imaging experiment. Specifically, we calculated the CRB associated with the three sets of acquisition parameters over different acquisition lengths. For all the experiments, we set $\text{SNR} = 33$ dB. In order to show the CRB for both T_1 and T_2 at the same scale, we used the normalized CRB defined as $\text{nCRB}_i = \sqrt{\text{CRB}(\theta_i)}/\theta_i$.

Fig. 4 shows the normalized CRB versus the acquisition length for the white matter ROI. As expected, for all three schemes, the nCRBs of T_1 and T_2 reduce as the acquisition length becomes longer. For T_1 , the nCRB rapidly approaches its asymptotic limit with short acquisitions for all three schemes. However, for T_2 , the conventional scheme needs much longer acquisition to attain a good nCRB. Note that this is consistent with the previous observations in [7]–[11], and suggests the sub-optimality of the conventional scheme from an estimation-theoretic perspective. In contrast, the two optimized schemes significantly improve the nCRB of T_2 , especially with short acquisition lengths. For example, at $N = 400$, the optimized experiments reduce the nCRB of T_2 by about a factor of two.

Also note that the nCRB for Optimized-I is better than for Optimized-II over all the acquisition lengths. This is as expected, since, with a smaller set of constraints, Optimized-I searches over a larger feasible space of acquisition parameters. Nonetheless, the difference between the two optimized schemes is quite small. In the supplementary material, we also show the CRB evaluation with respect to the gray matter ROI (marked in Fig. 1 (a)), from which we had similar observations.

4) *Evaluation of fully-sampled experiments*: We evaluated the fully-sampled MR fingerprinting experiments described in Section III (A). Note that this scenario exactly corresponds to the data model in (8), with which we calculated the CRB and performed experiment design. Specifically, we simulated the experiments at $N = 400$ and $\text{SNR} = 33$ dB, using the conventional scheme, Optimized-I, and Optimized-II. Fig. 5 shows the reconstructed T_1 and T_2 maps. As can be seen, the two optimized schemes improve the accuracy of both T_1 and T_2 , although the improvement is more significant for T_2 . Moreover, the performance of Optimized-I is slightly better than that of Optimized-II, consistent with the CRB prediction shown before.

We further investigated the bias-variance property of the reconstructed parameter maps. Specifically, we performed Monte Carlo (MC) simulations with 100 trials to calculate the bias, variance, and mean square error of the reconstructed parameter maps. For convenience, we normalized these quantities as follows: (1) normalized bias:

$$\text{NBias}_v = \hat{\mathbb{E}} \left[\left| \mathbf{I}_v - \hat{\mathbf{I}}_v \right| \right] / \mathbf{I}_v,$$

(2) normalized variance:

$$\text{NVar}_v = \sqrt{\hat{\mathbb{E}} \left[\left| \mathbf{I}_v - \hat{\mathbb{E}}(\mathbf{I}_v) \right|^2 \right]} / \mathbf{I}_v,$$

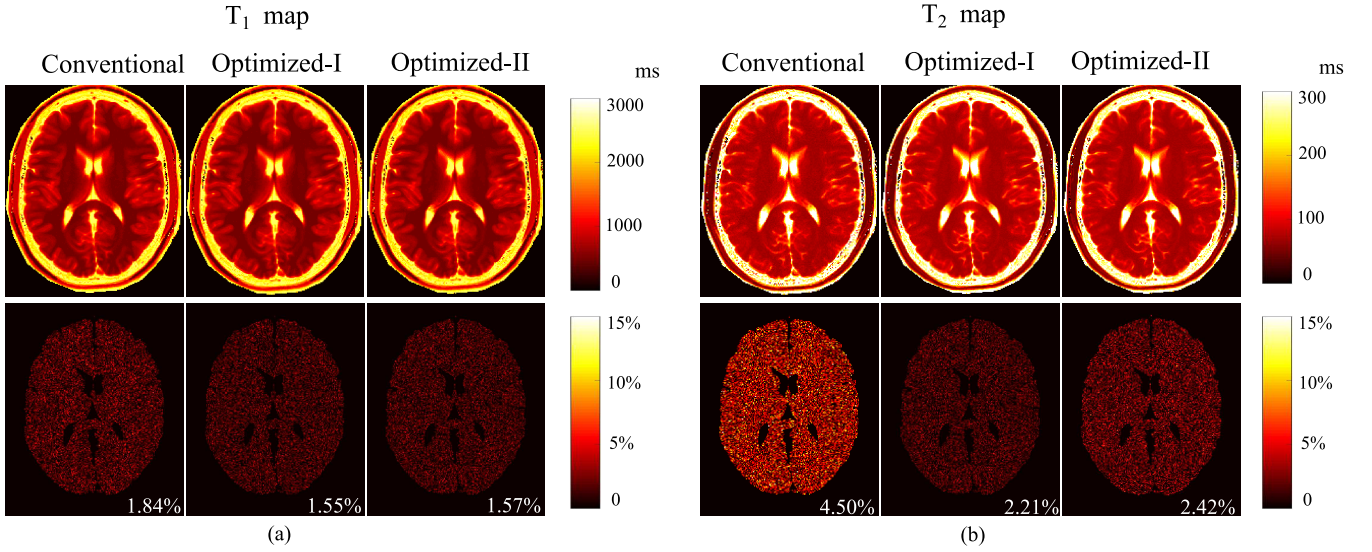


Fig. 5. Reconstructed parameter maps from the fully-sampled MR fingerprinting experiments ($N = 400$ and $\text{SNR} = 33$ dB), using the acquisition parameters from the conventional scheme, Optimized-I, and Optimized-II. (a) Reconstructed T_1 maps and associated relative error maps. (b) Reconstructed T_2 maps and associated relative error maps. Note that the overall error is labeled at the lower right corner of each error map, and the regions associated with the background, skull, scalp, and CSF were set to be zero.

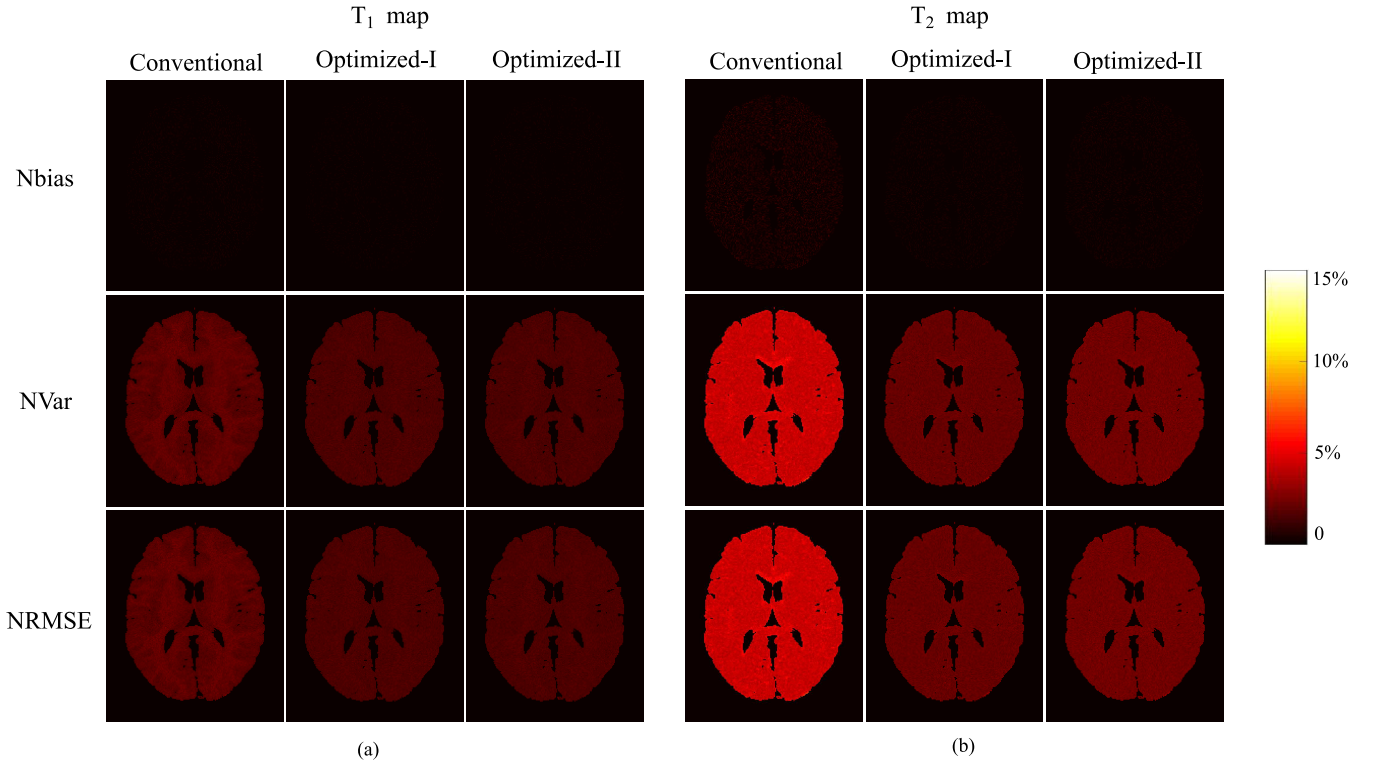


Fig. 6. Bias-variance analysis of the reconstructed parameter maps from the fully-sampled MR fingerprinting experiments ($N = 400$ and $\text{SNR} = 33$ dB), using the acquisition parameters from the conventional scheme, Optimized-I, and Optimized-II. (a) Normalized bias, variance, and root-mean-square error for (a) T_1 maps and (b) T_2 maps. The regions associated with the background, skull, scalp, and CSF were set to be zero.

and (3) normalized root-mean-square error:

$$\text{NRMSE}_v = \sqrt{\hat{\mathbb{E}} \left[\left| \mathbf{I}_v - \hat{\mathbf{I}}_v \right|^2 \right]} / \mathbf{I}_v,$$

where $\hat{\mathbb{E}}(\cdot)$ denotes the empirical mean evaluated for the MC simulations, and \mathbf{I}_v and $\hat{\mathbf{I}}_v$ respectively denote the v th voxel

from the true parameter map and reconstructed parameter map. Note that

$$\text{NRMSE}_n = \sqrt{\text{NBias}_n^2 + \text{NVar}_n^2}.$$

Fig. 6 shows the normalized bias, variance, and root-mean-square error maps for the reconstructed T_1 and T_2 maps. As can be seen, Optimized-I and Optimized-II reduce the

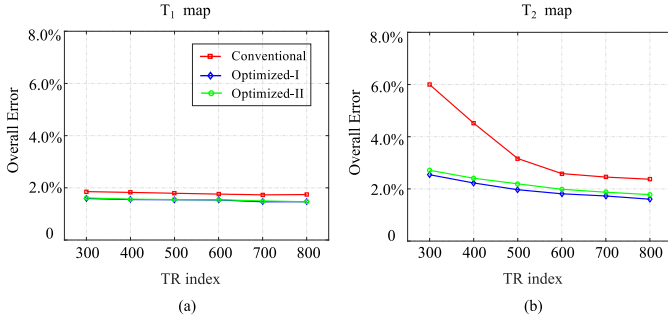


Fig. 7. Overall error versus the acquisition length for the fully-sampled MR fingerprinting experiments. (a) Overall error of T_1 map. (b) Overall error of T_2 map.

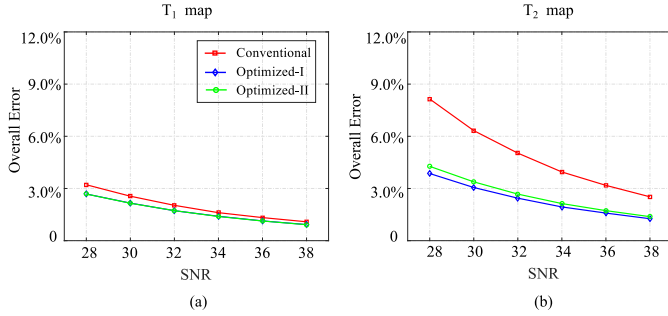


Fig. 8. Overall error versus the SNR level for the fully-sampled MR fingerprinting experiments. (a) Overall error of T_1 map. (b) Overall error of T_2 map.

normalized variances for both T_1 and T_2 , compared to the conventional scheme. Consistent with the CRB prediction and the results shown in Fig. 5, the improvement for T_2 is more substantial than for T_1 . Moreover, for all three acquisition schemes, the normalized variance is much larger than the normalized bias, and the normalized root-mean-square error is dominated by the normalized variance. Note that this is expected, since the ML reconstruction is asymptotically unbiased [13].

Moreover, we evaluated the fully-sampled experiments with different acquisition lengths, with N ranging from 300 to 800. Here we set $\text{SNR} = 33$ dB for the experiments. Fig. 7 shows the overall errors of T_1 and T_2 versus the acquisition length. Clearly, the two optimized acquisition schemes outperform the conventional scheme over all the acquisition lengths. As one more example, we show the reconstruction results for $N = 600$ in the supplementary material.

Finally, we evaluated the fully-sampled experiments with different SNR levels, ranging from 28 dB to 38 dB. Here we set at $N = 400$ for all the experiments. Fig. 8 shows the overall errors of T_1 and T_2 versus the SNR. As can be seen, the optimized acquisition schemes outperform the conventional scheme over all the SNR levels.

5) *Evaluation of highly-undersampled experiments:* We repeated the same evaluations but applied to the highly-undersampled case. Note that this more closely matches the way that MR fingerprinting is applied in practice. Fig. 9 shows the reconstructed T_1 and T_2 maps from the highly-undersampled experiments at $N = 400$ and $\text{SNR} = 33$ dB, us-

ing the conventional scheme, and the two optimized schemes. As can be seen, Optimized-I improves the accuracy of the T_2 map over the conventional scheme, but at the expense of degrading the accuracy of the T_1 map. In contrast, Optimized-II provides better accuracy for both T_1 and T_2 maps, which is highly desirable. Note that the ML reconstruction involves solving a nonlinear and nonconvex optimization problem, for which a good initialization is often required. By enforcing the additional constraint on the flip angle variations, Optimized-II results in much smoother magnetization evolutions (as shown in Fig. 3). With the highly-undersampled data, this often leads to better pattern matching results for the conventional reconstruction, which in turn provides an improved initialization for the ML reconstruction.

Fig. 10 shows the normalized bias, variance, and root-mean-square error maps for the reconstructed T_1 and T_2 maps from the MC simulations (with 100 trials). Clearly, Optimized-II reduces the normalized variance and root-mean-square error for both T_1 and T_2 maps, compared to the conventional scheme. Moreover, with smooth magnetization evolutions, Optimized-II reduces the bias compared to Optimized-I. This further illustrates the merit of introducing the constraint on the flip angle variations for the highly-undersampled experiments.

Fig. 11 shows the overall errors of T_1 and T_2 versus the acquisition length, for the highly-undersampled experiments with $\text{SNR} = 33$ dB. Clearly, Optimized-II outperforms the conventional scheme and Optimized-I for all the acquisition lengths. As a further illustration, we show the reconstruction results for $N = 600$ in the supplementary material.

Fig. 12 shows the overall errors of T_1 and T_2 versus the SNR, for the highly-undersampled experiments with $N = 400$. As can be seen, Optimized-II provides better accuracy than the conventional scheme and Optimized-I over all the SNR levels.

B. Phantom Experiments

We further evaluated the proposed approach using phantom experiments. Specifically, we created a physical phantom that consists of 9 plastic tubes, each one filled with a solution of Gadolinium and Agar at different concentrations. This created different combinations of T_1 and T_2 values that are relevant to the neuroimaging application [46]. We carried out the experiments on a 3T Siemens Tim Trio scanner (Siemens Medical Solutions, Erlangen, Germany) equipped with a 32-channel head array coil. The relevant imaging parameters include: $\text{FOV} = 300 \times 300$ mm², matrix size = 256×256 , and slice thickness = 5 mm.

Here we focus on the highly-undersampled MR fingerprinting experiments, which is of the most practical interest. Specifically, we performed two sets of experiments with $N = 400$, respectively, using the acquisition parameters from the conventional scheme and Optimized-II.⁹ We used the same spiral trajectory and sampling pattern as in the numerical simulations. Here the acquisition times for the conventional scheme and Optimized-II were 5.28 sec and

⁹Given that Optimized-II outperforms Optimized-I in highly-undersampled MR fingerprinting experiments, we only considered Optimized-II for our phantom experiments.

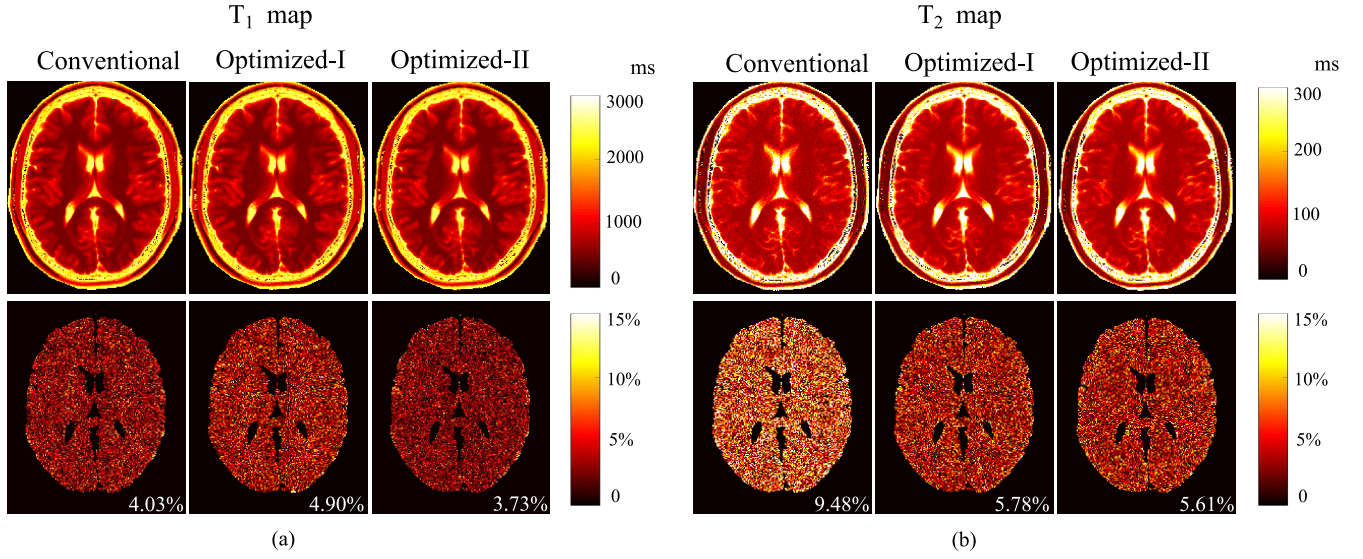


Fig. 9. Reconstructed parameter maps from the highly-undersampled MR fingerprinting experiments ($N = 400$ and $\text{SNR} = 33$ dB), using the acquisition parameters from the conventional scheme, Optimized-I, and Optimized-II. (a) Reconstructed T_1 maps and associated relative error maps. (b) Reconstructed T_2 maps and associated relative error maps. Note that the overall error is labeled at the lower right corner of each error map, and the regions associated with the background, skull, scalp, and CSF were set to be zero.

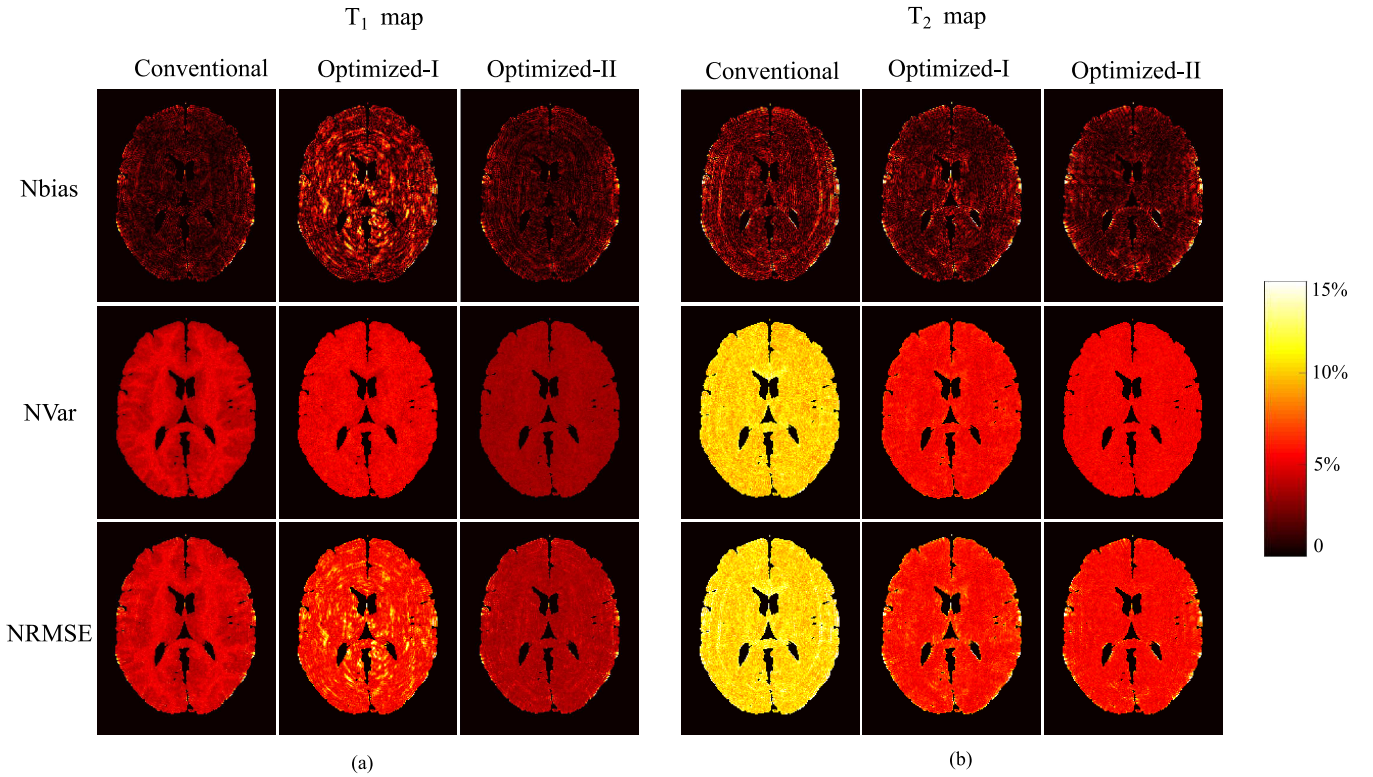


Fig. 10. Bias-variance analysis of the reconstructed parameter maps from the highly-undersampled MR fingerprinting experiments ($N = 400$ and $\text{SNR} = 33$ dB), using the acquisition parameters from the conventional scheme, Optimized-I, and Optimized-II. (a) Normalized bias, variance, and root-mean-square error for (a) T_1 maps and (b) T_2 maps. The regions associated with the background, skull, scalp, and CSF were set to be zero.

5.22 sec, respectively. To evaluate the performance of the above experiments, we also acquired a set of reference T_1 and T_2 maps, by performing a fully-sampled MR fingerprinting

experiment¹⁰ with $N = 1000$ using the acquisition parameters from the conventional scheme. The acquisition time for this

¹⁰The fully-sampled experiment was performed by repeating a highly-undersampled acquisition 48 times. For each acquisition, we switched to a different spiral interleaf at every time point. Note that a short time delay was added between consecutive acquisitions to ensure that the magnetization starts at thermal equilibrium.

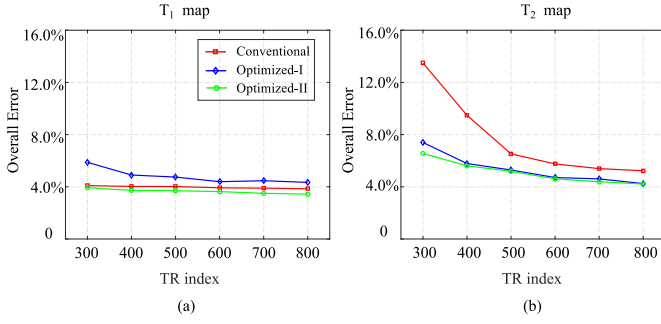


Fig. 11. Overall error versus the acquisition length for the highly-undersampled MR fingerprinting experiments. (a) Overall error of T_1 map. (b) Overall error of T_2 map.

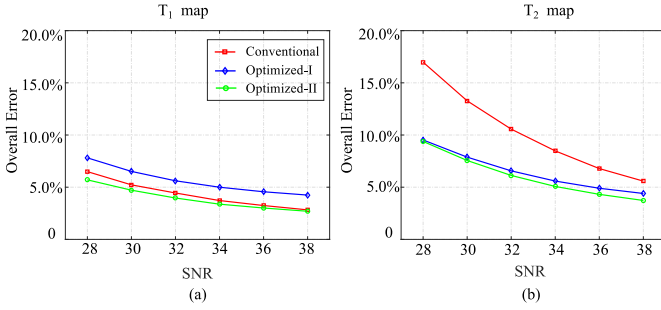


Fig. 12. Overall error versus the SNR level for the highly-undersampled MR fingerprinting experiments. (a) Overall error of T_1 map. (b) Overall error of T_2 map.

experiment was about 18 min. Additionally, we calibrated the spiral trajectory with a specialized pulse sequence [47] to avoid the potential trajectory distortion (caused by eddy currents and gradient delay). Finally, we performed an auxiliary scan with a gradient echo sequence, from which we estimated the coil sensitivity maps.

We performed the ML reconstruction for the above experiments, and used the same dictionary as in our numerical simulation. Fig. 13 shows the reconstructed T_1 and T_2 maps as well as the relative error maps (evaluated with respect to the reference data). Fig. 14 shows the corresponding reconstruction errors for each tube. As can be seen, Optimized-II significantly improves the accuracy of the T_2 map, while providing similar accuracy for the T_1 map.

IV. DISCUSSION

In this work, we used a simplified data model in (8) to calculate the CRB and to optimize acquisition parameters for MR fingerprinting. To tailor for highly-undersampled experiments, we further incorporated the constraint on the flip angle variation to enforce the smoothness of the magnetization evolution. The results from the numerical simulations and phantom experiments show the effectiveness of the proposed approach. As a generalization, it would be interesting to study the problem of jointly designing acquisition parameters and k -space trajectory. However, the CRB calculation in this case requires a substantially higher-dimensional formulation that models both contrast encoding and spatial encoding. This can be computationally more expensive.

For the experiment design problems in (18) and (19), we manually selected the parameters of the weighting matrix and the constraint sets. This provided good performance for the above application example. In general, we should choose these parameters according to application-specific requirements. For example, in cardiac MR fingerprinting experiments (e.g., [48]), we may want to constrain flip angles to be small, and apply multiple inversion preparation RF pulses during acquisition.

The proposed approach selected a few representative tissues to perform experiment design. This is feasible, since the range of tissue parameter values is often known a priori for a specific imaging application. In practice, this strategy generalizes well, as demonstrated in the numerical simulations and phantom experiments. From a Bayesian perspective, this is equivalent to assuming that there are a finite number of tissue types, and each tissue has the equal probability. With this viewpoint, we can generalize the proposed approach to incorporate a more complex probability distribution of tissues parameter values [30], and perform optimal experiment design with the Bayesian CRB [49]. Note that beyond the Bayesian paradigm, we can also use the min-max criterion [31] to design experiments, which minimizes the worst case performance.

By solving (18) and (19), we observed that the optimized acquisition parameters appeared to be highly structured. In particular, the optimized repetition times appeared to be binary. Note that such an interesting behavior is worth an in-depth study. As shown in [21], [50], certain CRB based experiment design problems that involve a dynamic system can be cast as optimal control problems, and it is possible that our empirical observations could be explained by the principles of optimal control theory [22], [51].¹¹ Although a control-theoretic characterization of (18) and (19) is beyond the scope of this paper, we believe that this is an interesting topic to follow up on. In particular, if we know in advance that (18) and (19) admit structured solutions, this fact could be leveraged to greatly simplify the algorithms used to derive an optimal experiment design.

In the application example, we illustrated the proposed approach by optimizing the flip angles and repetition times for the IR-FISP sequence. As a generalization, we can also include other acquisition parameters (e.g., RF pulse phases, echo times, etc). With a larger space of acquisition parameters, we could achieve better performance, although solving the associated optimization problem can become computationally more expensive. Moreover, beyond measuring tissue relaxation times, we could also design MR fingerprinting experiments to include other tissue parameters, such as apparent diffusion coefficients [52], magnetization transfer [53], etc.

The implementation described in this paper focused on optimizing the CRB for a fixed number of TRs. In practice, there are many other design considerations (e.g., acoustic characteristics of the pulse sequence [54], SAR, total acquisition

¹¹To the best of our knowledge, this work is the first that reports Bang-Bang structure for the optimized acquisition parameters in MR fingerprinting. Although Maidens et al. formulated the experiment design problem as an optimal control problem and derived an approximate dynamic programming algorithm [21], they only considered a highly-simplified problem setup and did not report the Bang-Bang behavior.

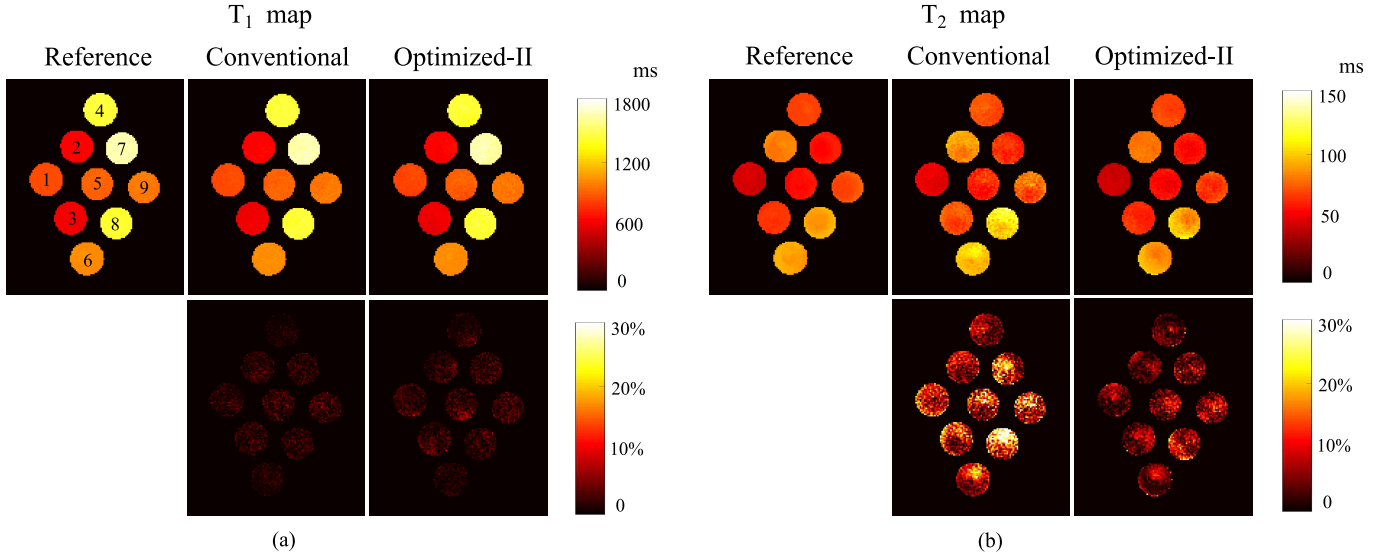


Fig. 13. Reconstructed parameter maps for the phantom experiments ($N = 400$) using the acquisition parameters from the conventional scheme, and Optimized-II. (a) Reconstructed T_1 map and associated relative error map. (b) Reconstructed T_2 map and associated relative error map. Note that the highly-undersampled MR fingerprinting experiments using the conventional scheme and optimized-II respectively took 5.28 sec and 5.22 sec, whereas the fully-sampled MR fingerprinting experiment for the reference data took 18.3 min.

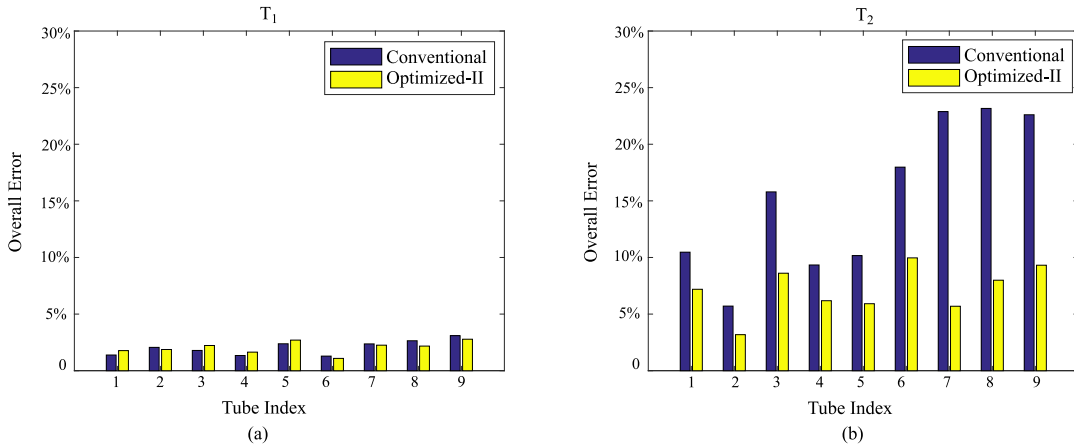


Fig. 14. Reconstruction errors for the phantom experiments ($N = 400$) using the acquisition parameters from the conventional scheme, and Optimized-II. (a) Overall error of the T_1 reconstruction at each tube. (b) Overall error of the T_2 reconstruction at each tube.

time, etc), which are important and may be worth including within the optimization framework. The extension to further include these considerations may further improve the practical significance of our approach.

V. CONCLUSION

In this work, we presented a novel estimation-theoretic approach to optimize acquisition parameters of MR fingerprinting experiments. The proposed approach maximizes the SNR efficiency of the resulting experiments, while incorporating constraints from the image decoding/reconstruction process. The optimized experiments enables substantially improved accuracy for T_2 maps, while providing slightly better or similar accuracy for T_1 maps. Remarkably, we found that the optimized acquisition parameters appear to be highly structured, rather than random/pseudo-randomly varying as used in the conventional MR fingerprinting experiments.

VI. APPENDIX

In this appendix, we derive the Jacobian matrix $\mathbf{J}_n(\theta)$ in (14) for the IR-FISP sequence. This provides an example to illustrate the procedure described in (15) and (16). Recall that in the IR-FISP sequence, $\theta = [T_1, T_2, M_0]^T$ and

$$\mathbf{J}_n(\theta) = \frac{\partial \mathbf{m}[n]}{\partial \theta} = \begin{bmatrix} \frac{\partial}{\partial T_1} \mathbf{m}[n] & \frac{\partial}{\partial T_2} \mathbf{m}[n] & \frac{\partial}{\partial M_0} \mathbf{m}[n] \end{bmatrix}.$$

For clarity, we first summarize the state-space model for the IR-FISP sequence as follows:

$$\mathbf{M}_r[n] = \mathbf{G}(\beta_r) \mathbf{R}(T_1, T_2, TR_n) \mathbf{Q}(\alpha_n, \phi_n) \mathbf{M}_r[n-1] + \frac{M_0}{N_v} \mathbf{b}(T_1, TR_n), \quad (20)$$

$$\mathbf{m}[n] = \sum_r \mathbf{P} \mathbf{R}(T_1, T_2, TE_n) \mathbf{Q}(\alpha_n, \phi_n) \mathbf{M}_r[n-1], \quad (21)$$

for $n = 1, \dots, N$. Next, we calculate the derivatives of $\mathbf{m}[n]$ with respect to T_1 , T_2 , and M_0 based on (15) and (16).

A. Derivative of \mathbf{m}^n with respect to T_1

Invoking the derivative with respect to T_1 on both sides of (21), we have

$$\frac{\partial \mathbf{m}[n]}{\partial T_1} = \sum_{\mathbf{r}} \left\{ \mathbf{P} \frac{\partial \mathbf{R}(T_1, T_2, TE_n)}{\partial T_1} \mathbf{Q}(\alpha_n, \phi_n) \mathbf{M}_{\mathbf{r}}[n-1] + \mathbf{P} \mathbf{R}(T_1, T_2, TE_n) \mathbf{Q}(\alpha_n, \phi_n) \frac{\partial \mathbf{M}_{\mathbf{r}}[n-1]}{\partial T_1} \right\}, \quad (22)$$

where

$$\frac{\partial \mathbf{R}(T_1, T_2, TE_n)}{\partial T_1} = \frac{TE_n}{T_1^2} \exp\left(-\frac{TE_n}{T_1}\right) \begin{bmatrix} 0 & 0 & 0 \\ 0 & 0 & 0 \\ 0 & 0 & 1 \end{bmatrix}.$$

Noting that

$$\mathbf{P} \frac{\partial \mathbf{R}(T_1, T_2, TE_n)}{\partial T_1} = \mathbf{0},$$

(22) can be simplified as

$$\frac{\partial \mathbf{m}[n]}{\partial T_1} = \sum_{\mathbf{r}} \mathbf{P} \mathbf{R}(T_1, T_2, TE_n) \mathbf{Q}(\alpha_n, \phi_n) \frac{\partial \mathbf{M}_{\mathbf{r}}[n-1]}{\partial T_1}. \quad (23)$$

We then take the derivative with respect to T_1 on both sides of (20), i.e.,

$$\begin{aligned} \frac{\partial \mathbf{M}_{\mathbf{r}}[n]}{\partial T_1} &= \mathbf{G}(\beta_{\mathbf{r}}) \frac{\partial \mathbf{R}(T_1, T_2, TR_n)}{\partial T_1} \mathbf{Q}(\alpha_n, \phi_n) \mathbf{M}_{\mathbf{r}}[n-1] \\ &+ \mathbf{G}(\beta_{\mathbf{r}}) \mathbf{R}(T_1, T_2, TR_n) \mathbf{Q}(\alpha_n, \phi_n) \frac{\partial \mathbf{M}_{\mathbf{r}}[n-1]}{\partial T_1} \\ &+ \frac{M_0}{N_v} \frac{\partial b(T_1, TR_n)}{\partial T_1}, \end{aligned} \quad (24)$$

where

$$\frac{\partial \mathbf{R}(T_1, T_2, TR_n)}{\partial T_1} = \frac{TR_n}{T_1^2} \exp\left(-\frac{TR_n}{T_1}\right) \begin{bmatrix} 0 & 0 & 0 \\ 0 & 0 & 0 \\ 0 & 0 & 1 \end{bmatrix},$$

and

$$\frac{\partial b(T_1, TR_n)}{\partial T_1} = -\frac{TR_n}{T_1^2} \exp\left(-\frac{TR_n}{T_1}\right).$$

Here we can calculate $\partial \mathbf{m}[n]/\partial T_1$ by iterating (23) and (24) with the initial conditions $\mathbf{M}_{\mathbf{r}}[0] = \frac{M_0}{N_v} [0 \ 0 \ 1]^T$ and $\partial \mathbf{M}_{\mathbf{r}}[0]/\partial T_1 = [0 \ 0 \ 0]^T$.

B. Derivative of \mathbf{m}^n with respect to T_2

Invoking the derivative respect to T_2 on both sides of (21), we have

$$\begin{aligned} \frac{\partial \mathbf{m}[n]}{\partial T_2} &= \sum_{\mathbf{r}} \left\{ \mathbf{P} \frac{\partial \mathbf{R}(T_1, T_2, TE_n)}{\partial T_2} \mathbf{Q}(\alpha_n, \phi_n) \mathbf{M}_{\mathbf{r}}[n-1] \right. \\ &\left. + \mathbf{P} \mathbf{R}(T_1, T_2, TE_n) \mathbf{Q}(\alpha_n, \phi_n) \frac{\partial \mathbf{M}_{\mathbf{r}}[n-1]}{\partial T_2} \right\}, \end{aligned} \quad (25)$$

where

$$\frac{\partial \mathbf{R}(T_1, T_2, TE_n)}{\partial T_2} = \frac{TE_n}{T_2^2} \exp\left(-\frac{TE_n}{T_2}\right) \begin{bmatrix} 1 & 0 & 0 \\ 0 & 1 & 0 \\ 0 & 0 & 0 \end{bmatrix}.$$

We then take the derivative with respect to T_2 on both sides of (20), i.e.,

$$\begin{aligned} \frac{\partial \mathbf{M}_{\mathbf{r}}[n]}{\partial T_2} &= \mathbf{G}(\beta_{\mathbf{r}}) \frac{\partial \mathbf{R}(T_1, T_2, TR_n)}{\partial T_2} \mathbf{Q}(\alpha_n, \phi_n) \mathbf{M}_{\mathbf{r}}[n-1] \\ &+ \mathbf{G}(\beta_{\mathbf{r}}) \mathbf{R}(T_1, T_2, TR_n) \mathbf{Q}(\alpha_n, \phi_n) \frac{\partial \mathbf{M}_{\mathbf{r}}[n-1]}{\partial T_2}, \end{aligned} \quad (26)$$

where

$$\frac{\partial \mathbf{R}(T_1, T_2, TR_n)}{\partial T_2} = \frac{TR_n}{T_2^2} \exp\left(-\frac{TR_n}{T_2}\right) \begin{bmatrix} 1 & 0 & 0 \\ 0 & 1 & 0 \\ 0 & 0 & 0 \end{bmatrix}.$$

Here we can calculate $\partial \mathbf{m}[n]/\partial T_2$ by iterating (25) and (26) with the initial conditions $\mathbf{M}_{\mathbf{r}}[0] = \frac{M_0}{N_v} [0 \ 0 \ 1]^T$ and $\partial \mathbf{M}_{\mathbf{r}}[0]/\partial T_2 = [0 \ 0 \ 0]^T$.

C. Derivative of \mathbf{m}^n with respect to M_0

Invoking the derivative with respect to M_0 on both sides of (21), we have

$$\frac{\partial \mathbf{m}[n]}{\partial M_0} = \sum_{\mathbf{r}} \mathbf{P} \mathbf{R}(T_1, T_2, TE_n) \mathbf{Q}(\alpha_n, \phi_n) \frac{\partial \mathbf{M}_{\mathbf{r}}[n-1]}{\partial M_0}. \quad (27)$$

We then take the derivative with respect to M_0 on both sides of (20), i.e.,

$$\begin{aligned} \frac{\partial \mathbf{M}_{\mathbf{r}}[n]}{\partial M_0} &= \mathbf{G}(\beta_{\mathbf{r}}) \mathbf{R}(T_1, T_2, TR_n) \mathbf{Q}(\alpha_n, \phi_n) \frac{\partial \mathbf{M}_{\mathbf{r}}[n-1]}{\partial M_0} \\ &+ \frac{1}{N_v} b(T_1, TR_n). \end{aligned} \quad (28)$$

Here we can calculate $\partial \mathbf{m}[n]/\partial M_0$ by iterating (27) and (28) with the initial condition $\partial \mathbf{M}_{\mathbf{r}}[0]/\partial M_0 = \frac{1}{N_v} [0 \ 0 \ 1]^T$.

REFERENCES

- [1] D. Ma, V. Gulani, N. Seiberlich, K. Liu, J. L. Sunshine, J. L. Duerk, and M. A. Griswold, "Magnetic resonance fingerprinting," *Nature*, vol. 495, pp. 187–192, 2013.
- [2] K. Scheffler and J. Hennig, "T1 quantification with inversion recovery TrueFISP," *Magn. Reson. Med.*, vol. 45, pp. 720–723, 2001.
- [3] S. C. Deoni, B. K. Rutt, and T. M. Peters, "Rapid combined T1 and T2 mapping using gradient recalled acquisition in the steady state," *Magn. Reson. Med.*, vol. 49, pp. 515–526, 2003.
- [4] P. Schmitt, M. A. Griswold, P. M. Jakob, M. Kotas, V. Gulani, M. Flentje, and A. Haase, "Inversion recovery TrueFISP: Quantification of T1, T2, and spin density," *Magn. Reson. Med.*, vol. 51, pp. 661–667, 2004.
- [5] J. Warntjes, O. Dahlqvist, and P. Lundberg, "Novel method for rapid, simultaneous T1, T2*, and proton density quantification," *Magn. Reson. Med.*, vol. 57, pp. 528–537, 2007.
- [6] M. Davies, G. Puy, P. Vandergheynst, and Y. Wiaux, "A compressed sensing framework for magnetic resonance fingerprinting," *SIAM J. Imaging Sciences*, vol. 7, pp. 2623–2656, 2014.
- [7] B. Zhao, F. Lam, B. Bilgic, H. Ye, and K. Setsompop, "Maximum likelihood reconstruction for magnetic resonance fingerprinting," in *Proc. IEEE Int. Symp. Biomed. Imaging*, 2015, pp. 905–909.
- [8] B. Zhao, K. Setsompop, H. Ye, S. Cauley, and L. L. Wald, "Maximum likelihood reconstruction for magnetic resonance fingerprinting," *IEEE Trans. Med. Imaging*, vol. 35, pp. 1812–1823, 2016.
- [9] E. Y. Pierre, D. Ma, Y. Chen, C. Badve, and M. A. Griswold, "Multiscale reconstruction for MR fingerprinting," *Magn. Reson. Med.*, vol. 75, pp. 2481–2492, 2016.
- [10] X. Cao, C. Liao, Z. Wang, Y. Chen, H. Ye, H. He, and J. Zhong, "Robust sliding-window reconstruction for accelerating the acquisition of MR fingerprinting," *Magn. Reson. Med.*, vol. 78, pp. 1579–1588, 2017.

- [11] B. Zhao, K. Setsompop, E. Adalsteinsson, B. Gagoski, H. Ye, D. Ma, Y. Jiang, P. E. Grant, M. A. Griswold, and L. L. Wald, "Improved magnetic resonance fingerprinting reconstruction with low-rank and subspace modeling," *Magn. Reson. Med.*, 2017, in press.
- [12] F. Pukelsheim, *Optimal Design of Experiments*. New York: John Wiley and Sons, 1993.
- [13] S. M. Kay, *Fundamentals of Statistical Signal Processing: Estimation Theory*. Upper Saddle River, NJ: Prentice Hall, 1993, vol. I.
- [14] Y. Jiang, D. Ma, N. Seiberlich, V. Gulani, and M. A. Griswold, "MR fingerprinting using fast imaging with steady state precession (FISP) with spiral readout," *Magn. Reson. Med.*, vol. 74, pp. 1621–1631, 2015.
- [15] J. Assländer, S. J. Glaser, and J. Hennig, "Pseudo steady-state free precession for MR-fingerprinting," *Magn. Reson. Med.*, vol. 77, pp. 1151–1161, 2017.
- [16] Y. Jiang, D. Ma, R. Jerecic, J. Duerk, N. Seiberlich, V. Gulani, and M. A. Griswold, "MR fingerprinting using the quick echo splitting NMR imaging technique," *Magn. Reson. Med.*, vol. 77, pp. 979–988, 2017.
- [17] B. Rieger, F. Zimmer, J. Zapp, S. Weingärtner, and L. R. Schad, "Magnetic resonance fingerprinting using echo-planar imaging: Joint quantification of T1 and T2* relaxation times," *Magn. Reson. Med.*, vol. 77, pp. 979–988, 2017.
- [18] B. Zhao, J. P. Haldar, K. Setsompop, and L. L. Wald, "Towards optimized experiment design for magnetic resonance fingerprinting," in *Proc. Int. Symp. Magn. Reson. Med.*, 2016, p. 2835.
- [19] —, "Optimal experiment design for magnetic resonance fingerprinting," in *Proc. IEEE Eng. Med. Bio. Conf.*, 2016, pp. 453–456.
- [20] J. Assländer, D. Sodickson, R. Lattanzi, and M. Cloos, "Relaxation in polar coordinates: Analysis and optimization of MR-fingerprinting," in *Proc. Int. Symp. Magn. Reson. Med.*
- [21] J. Maidens, A. Packard, and M. Arcak, "Parallel dynamic programming for optimal experiment design in nonlinear systems," in *55th IEEE Conf. on Decision and Control*, 2016, pp. 2894–2899.
- [22] D. P. Bertsekas, *Dynamic Programming and Optimal Control*. Belmont, MA: Athena Scientific, 2017, vol. I.
- [23] O. Cohen and M. S. Rosen, "Algorithm comparison for schedule optimization in MR fingerprinting," *Magn. Reson. Imaging*, vol. 41, pp. 15–21.
- [24] J. A. Jones, P. Hodgkinson, A. L. Barker, and P. J. Hore, "Optimal sampling strategies for the measurement of spin-spin relaxation times," *J. Magn. Reson. Ser. B*, vol. 113, pp. 25–34, 1996.
- [25] Y. Zhang, H. N. Yeung, M. O'Donnell, and P. L. Carson, "Determination of sample time for T1 measurement," *J. Magn. Reson. Imaging*, vol. 8, pp. 675–681, 1998.
- [26] J. P. Haldar, D. Hernando, and Z.-P. Liang, "Super-resolution reconstruction of MR image sequences with contrast modeling," in *Proc. IEEE Int. Symp. Biomed. Imaging*, 2009, pp. 266–269.
- [27] A. Funai and J. A. Fessler, "Cramér Rao bound analysis of joint B1/T1 mapping methods in MRI," in *Proc. IEEE Int. Symp. Biomed. Imaging*, 2010, pp. 712–715.
- [28] B. Zhao, F. Lam, and Z.-P. Liang, "Model-based MR parameter mapping with sparsity constraints: Parameter estimation and performance bounds," *IEEE Trans. Med. Imaging*, vol. 33, pp. 1832–1844, 2014.
- [29] M. Akçakaya, S. Weingärtner, S. Roujol, and R. Nezafat, "On the selection of sampling points for myocardial T1 mapping," *Magn. Reson. Med.*, vol. 73, pp. 1741–1753, 2015.
- [30] C. M. Lewis, S. A. Hurley, M. E. Meyerand, and C. G. Koay, "Data-driven optimized flip angle selection for T1 estimation from spoiled gradient echo acquisitions," *Magn. Reson. Med.*, vol. 76, pp. 792–802, 2016.
- [31] G. Nataraj, J. F. Nielsen, and J. A. Fessler, "Optimizing MR scan design for model-based T1, T2 estimation from steady-state sequences," *IEEE Trans. Med. Imaging*, vol. 36, pp. 467–477, 2017.
- [32] R. P. A. Teixeira, S. J. Malik, and J. V. Hajnal, "Joint system relaxation (JSR) and Cramér-Rao lower bound optimization of sequence parameters: A framework for enhanced precision of DESPOT T1 and T2 estimation," *Magn. Reson. Med.*, 2017, in press.
- [33] D. Luenberger, *Introduction to Dynamic Systems: Theory, Models, and Applications*. NY: John Wiley & Sons, 1979.
- [34] F. Bloch, "Nuclear induction," *Phys. Rev.*, vol. 70, pp. 460–474, 1946.
- [35] P. Shkarin and R. G. Spencer, "Time domain simulation of Fourier imaging by summation of isochromats," *Int. J. Imag. Syst. Tech.*, vol. 8, pp. 419–426, 1997.
- [36] S. J. Malik, A. Sbrizzi, H. Hoogduin, and J. V. Hajnal, "Equivalence of EPG and isochromat-based simulation of MR signals," in *Proc. Int. Symp. Magn. Reson. Med.*, 2016, p. 3196.
- [37] Z.-P. Liang and P. C. Lauterbur, *Principles of Magnetic Resonance Imaging: A Signal Processing Perspective*. New York: IEEE Press/Wiley, 1999.
- [38] B. Zhao, "Model-based iterative reconstruction for magnetic resonance fingerprinting," in *Proc. IEEE Int. Conf. Image Process.*, 2015, pp. 3392–3396.
- [39] J. Nocedal and S. J. Wright, *Numerical Optimization*. NY: Springer, 2006.
- [40] J. C. Spall, *Introduction to Stochastic Search and Optimization: Estimation, Simulation, and Control*. NY: John Wiley & Sons, 2003.
- [41] D. L. Collins, A. P. Zijdenbos, V. Kollokian, J. G. Sled, N. J. Kabani, C. J. Holmes, and A. C. Evans, "Design and construction of a realistic digital brain phantom," *IEEE Trans. Med. Imaging*, vol. 17, pp. 463–468, 1998.
- [42] M. Weigel, "Extended phase graphs: Dephasing, RF pulses, and echoes - pure and simple," *J. Magn. Reson. Imaging*, vol. 41, pp. 266–295, 2015.
- [43] J. A. Fessler and B. P. Sutton, "Nonuniform fast Fourier transforms using min-max interpolation," *IEEE Trans. Signal Process.*, vol. 51, pp. 560–574, 2003.
- [44] Y. Gao, Y. Chen, D. Ma, Y. Jiang, K. A. Herrmann, J. A. Vincent, K. M. Dell, M. L. Drumm, S. M. Brady-Kalnay, M. A. Griswold, C. A. Flask, and L. Lu, "Preclinical MR fingerprinting (MRF) at 7 T: Effective quantitative imaging for rodent disease models," *NMR Biomed.*, vol. 28, pp. 384–394, 2015.
- [45] J. P. Haldar, J. Anderson, and S. W. Sun, "Maximum likelihood estimation of T1 relaxation parameters using VARPRO," in *Proc. Int. Symp. Magn. Reson. Med.*, 2007, p. 41.
- [46] K. Hattori, Y. Ikemoto, W. Takao, S. Ohno, T. Harimoto, S. Kanazawa, M. Oita, K. Shibuya, M. Kuroda, and H. Kato, "Development of MRI phantom equivalent to human tissues for 3.0-T MRI," *Med. Phys.*, vol. 40, p. 032303, 2013.
- [47] H. Tan and C. H. Meyer, "Estimation of k-space trajectories in spiral MRI," *Magn. Reson. Med.*, vol. 61, pp. 1396–1404, 2009.
- [48] J. I. Hamilton, Y. Jiang, Y. Chen, D. Ma, W.-C. Lo, M. Griswold, and N. Seiberlich, "MR fingerprinting for rapid quantification of myocardial T1, T2, and proton spin density," *Magn. Reson. Med.*, vol. 77, pp. 1446–1458, 2017.
- [49] H. L. Van Trees and K. L. Bell, *Bayesian Bounds for Parameter Estimation and Nonlinear Filtering/Tracking*. New York: Wiley-IEEE Press, 2007.
- [50] R. T. N. Chen, "Input design for aircraft parameter identification: Using time-optimal control formulation," in *Methods for Aircraft State and Parameter Identification, Advisory Group for Aerospace Research and Development (AGARD), Conference Proceedings*, no. 172, 1975.
- [51] N. P. Osmolovskii and H. Maurer, *Applications to Regular and Bang-Bang Control: Second-Order Necessary and Sufficient Optimality Conditions in Calculus of Variations and Optimal Control*. Philadelphia, PA: SIAM, 2012.
- [52] Y. Jiang, D. Ma, K. Wright, N. Seiberlich, V. Gulani, and M. A. Griswold, "Simultaneous T1, T2, diffusion and proton density quantification with MR fingerprinting," in *Proc. Int. Symp. Magn. Reson. Med.*, 2014, p. 28.
- [53] T. Hilbert, T. Kober, T. Zhao, T. K. Block, Z. Yu, J.-P. Thiran, G. Krueger, D. K. Sodickson, and M. Cloos, "Mitigating the effect of magnetization transfer in magnetic resonance fingerprinting," in *Proc. Int. Symp. Magn. Reson. Med.*, 2017, p. 74.
- [54] D. Ma, E. Y. Pierre, Y. Jiang, M. D. Schluchter, K. Setsompop, V. Gulani, and M. A. Griswold, "Music-based magnetic resonance fingerprinting to improve patient comfort during MRI examinations," *Magn. Reson. Med.*, vol. 75, pp. 2303–2314, 2016.